Computers and Mathematics with Applications 175 (2024) 184–201

Contents lists available at ScienceDirect

Computers and Mathematics with Applications

journal homepage: www.elsevier.com/locate/camwa

Flow through a prosthetic mechanical aortic valve: Numerical model and experimental study

Marcin Nowak [a,*], Eduardo Divo [b], Tomasz Borkowski [c], Ewelina Marciniak [c], Marek Rojczyk [d], Ryszard Białecki [d]

[a] Gdańsk University of Technology, Faculty of Civil and Environmental Engineering, Department of Mechanics of Materials and Structures, Poland
[b] Mechanical Engineering Department, Embry-Riddle Aeronautical University, Orlando, FL, United States of America
[c] Medical University of Gdańsk, Faculty of Pharmacy, Department of Medical Laboratory Diagnostics-Fahrenheit Biobank BBMRI, Poland
[d] Silesian University of Technology, Department of Thermal Technology, Poland

ARTICLE INFO

Keywords:
Aortic valve
Test rig
Numerical model
Moving mesh
Computer vision
Social safety

ABSTRACT

This research presents a numerical model dedicated for virtual patient diagnostics in the field of synthetic valve implantation. The model operates based on computational fluid dynamics solver with implemented rigid body motion solver. Characteristic indicators related to the prosthetic valve were determined to assess the correctness of cardiac system operation after implantation. A novel approach for dynamic time discretization was developed for reliable and time-efficient calculation. The solver efficiency and computational savings due to application of the developed time-discretization scheme is discussed. Numerical results were validated using experimental data acquired from a test rig, including mass flow meter, pressure transducers, and valve holder designed for this purpose. Multivariant analysis of the model constant was performed towards different levels of the valve resistance to motion. The in-house algorithm was prepared to automatically determine the prosthetic valve position from fast camera images.

1. Introduction

Cardiovascular disease (CVD) was responsible for 31% of deaths in 2015, Each year CVD causes 3.9 million deaths in Europe, of which 1.8 million deaths are in the European Union [1–3]. One of the most life-threatening diseases is severe aortic valve stenosis, which prevails in older patients [4]. The survival reaches 50% in 5 years in the case of asymptomatic aortic stenosis, and in 2 years in the case of symptomatic stenosis [5]. Different methods are available for noninvasive diagnostics in cardiology, such as: echocardiography 3D/4D, computed tomography and cardiac magnetic resonance imaging. Unfortunately, each technique suffers from imperfections [6–9]. The shortcomings of the diagnostics techniques are dependent on the chosen method, and the examplary ones are: susceptibility to generate image rich in artifacts, costs, requirement of specially trained staff and complex facilities, radiation hazard, or the need to introduce contrast agent. Therefore, there is a room for improvement of diagnostic procedures, for example, using the hybrid approach that integrates diagnostic methods with numerical methods, that apply Computational Fluid Dynamics (CFD) [10,11] or Fluid-Structure Interaction (FSI) [12]. Substantial potential can be seen in CFD modeling, in terms of patient examination, treatment planning, finding cardiovascular zones susceptible to disease, anticipating surgery results, and designing medical devices. Furthermore, it could provide a useful response for surgeons for the choice of the best valve prosthesis and for manufacturers to reduce production costs [13–15].

The use of the FSI method is advantageous in the modeling of human or deformable artificial valves and arteries [16–19]. Different approaches can be found for FSI, the choice of which depends on the level of fluid-solid coupling, geometry complexity, deformations, and computer resources. For example, the partitioned approach includes two separate solvers (fluid solver and mechanical solver) and a module that couples each other. Exemplary usage can be found in [20], based on the application of the commercial Ansys® software. An application of the FSI procedure for modeling highly flexible bodies was presented in [21]. Arbitrary Lagrangian-Eulerian (ALE) approach [22–24] allows us to analyze the full FSI problem using one *monolitic* solver. However, this method requires the long computational time that results from solving the monolithic matrix, and the problem is ill-conditioned [25]. Research [26] performed a serie of 11 FSI analyses using patient-specific

* Corresponding author.
E-mail addresses: marcin.nowak1@pg.edu.pl, marcin9.nowak3@gmail.com (M. Nowak).

https://doi.org/10.1016/j.camwa.2024.09.010
Received 1 April 2024; Received in revised form 11 August 2024; Accepted 15 September 2024

geometric models, to analyze the validity of the fractional flow reserve criterion on the coronary intervention surgery. Based on calculations performed, it was recommended to use CFD as a complementary tool for patients, particularly for those with moderate stenosis.

An example of fully coupled FSI usage for a mechanical valve can be found in [27], where Comsol Multiphysics software was used to study the influence of hematocrit on the hemodynamics of the artificial heart valve. More novel methods - Immersed Boundary Method (IBM) and Lattice Boltzmann Method (LBM) enable more stable FSI computing [28–30]. An exemplary usage is the work of [31], where the curvilinear IBM was used to model the interaction between leaflets and blood flow. The LBM for hemodynamics is less commonly used and the exemplary work [32] considered the FSI of blood flow through the patient-specific cerebral vasculature.

All mentioned approaches have one common feature, namely, the computational cost is quite large, and as was mentioned, the stability of the coupling procedure in terms of usage the FSI approach is very problematic. Some perspective to replace long computational analysis is found in the usage of machine learning tools [33,34]. Also, the computational time and stability is considered more advantageous when the six Degrees of Freedom (6DOF) model is used [35].

The analysis of bileaflet 27 mm inner diameter valve was performed by [13], using ALE approach and experimental measurements. The test rig was equipped with piston-in-cylinder pumps and a system that mimicked the left ventricle. The predicted closing times and transvalvular pressure drops agreed with the validation data, falling in a range of two times the standard deviation. Research [36] used approach to analyze leaflet kinematics with different aortic root geometry applied. The results revealed that flow dynamics is more dominated by the valve configuration than by the aortic root shape, because the valve forces three-jet behavior and vortex shedding. The aortic root geometry and resulting bileaflet valve operation was also investigated by [37], where curvilinear, immersed-boundary FSI (CURVIB-FSI) was used along with measurements. The results showed that leaflets in the anatomic aorta open much faster and undergo a greater rebound during closing than the same valve in the straight axisymmetric aorta. The rebound effect differs in the studies of mechanical valves and it can be absent or visible up to a level of 12 degrees [27,31,38,39]. The validation of the numerical model for the flow analysis through the arteries with stent can be found in [40].

In this research, the flow mechanics through an artificial bileaflet mechanical valve was investigated using in-house 6DOF model with the adaptive timestepping method. Ansys® Fluent finite volume solver was used to solve partial differential equations within the finite volume method. To absorb valve motion in the numerical mesh, two different strategies of moving mesh were adopted and used: overset mesh and dynamic mesh. The results were compared with measurement data gained using in-house test rig with pressure and flow meters, a fast camera and prepared own LabView® control application. This is the next stage of authors research [41], where the validation was performed based on the literature data. The fast camera images were processed for the leaflets angular position, using Python Open Source Computer Vision Library (OpenCV) [42]. This is currently a novel approach in terms of artificial valve measurements. The model sensitivity to the moment of inertia error was quantified via performing a series of numerical simulations.
The novelty of this research is the application of the dynamic time discretization within the aortic valve modeling, which let it to decrease the demanded computational time substantially and avoid moving mesh errors [43]. Such an approach could be applied within the wide range of problems regarding the fluid or structural mechanics, reducing the solving time and improving the solver convergence. The moving mesh modules were compared, towards differences between results of models using them, their validity, susceptibility to errors and utility. This comparison was not previously investigated for mechanical valves in the literature.

2. Geometry and numerical mesh

Aortic valve geometry was created based on the user manual provided with device documentation [44]. The considered mechanical bileaflet valve's inside diameter is 16.8 mm. The leaflet shape is non-semicircular, because when the closed state is achieved, the angle between the leaflet and the inlet surface is equal to 25° - not 0° (Fig. 1D). Thus, to obtain the proper shape and chamferings, two semicircular leaflets were created at 25° angle (closed state) and with a radius two times exceeding the valve's inside diameter. Then, the slice extrusion operation based on the auxiliary cylinder with the desirable inside diameter was performed to cut out the excess leaflet fragments.

The three-dimensional background geometry prepared for the numerical model is simply a tube, representing the frame where the valve was fastened and the fragment of the test rig pipe (Fig. 1). The inside diameter equals 1.7 cm. The pipe length after the valve location, equals to 5.75 cm, is corresponding to the location of the 2nd pressure sensor. The length before the valve (13.4 cm) was used as shorter than the valve distance to the flow meter section, as it was investigated, by a series of simulations, that the limiting of this length does not influence the results. This is caused by the fact that the test rig tubes are non-deformable, so pressure wave propagation does not occur, and the used length is already sufficient to realize a hydraulic run. The location of the valve in the pipe can be observed in Fig. 1.

Several operations were demanded in terms of geometry and numerical mesh preparation. For the overset mesh, additional geometries for the component meshes (leaflets surroundings) have to be prepared. Each of the leaflets were extruded in its normal direction with an applied thickness of 2.25 mm, to create two separate surrounding geometries, one for each leaflet. The component meshes were created with cell growth rates ensuring the increasing cell size going from all leaflets walls and the appropriate quality parameters (Fig. 1). This was tested on the closed valve geometries, to adjust discretization toward proper operation during small gaps occurrence. The donor priority was set as boundary-distance and both components body priority was applied. In this way, the densified mesh was preserved in the vicinity of the leaflets (Fig. 1 (c)-(e)), which also allowed for better boundary layer resolving.

The overset background mesh was prepared as discretized pipe geometry using swept hexahedral cells with the 7-layer inflated prism boundary, with smooth cell size transition between the boundary and inner mesh. This was set to better resolve the boundary layer and ensure a proper number of cells across the gap, to avoid orphan cells when the valve is closed. The number of inflation layers resulted from the trials with the different number of layers applied, until the proper matching between the overset component and background meshes was achieved and no orphan cells were present. This purpose was achieved with the 7-, 8- and 9- layer prism boundary, from which the 7-layer mesh was chosen, to limit the number of cells.

To check the influence of domain discretization on the predicted results, the mesh sensitivity analysis was performed on three different meshes. Firstly, the overset mesh connectivity was tested with the entire range of leaflet angle using UDF `define_cg_motion`. The corresponding background and component mesh settings and densities were adjusted until the orphan cells were not present at any leaflet position. Three different mesh densities were prepared for the sensitivity analysis: *coarse* (background 881.000 cells, component 31.000 cells), *medium* (background 1.850.000 cells, component 55.000 cells) and *fine* (background 2.300.000 cells, component 94.000 cells). The leaflet motion and velocity values were compared for different meshes. Finally, the conclusion was made that further decrease in cell size does not influence the results and the *medium* mesh configuration was chosen for the analysis.

3. Moving mesh

There are different approaches to capture body movement, as: sliding mesh, dynamic mesh and the overset mesh [45]. The overset mesh

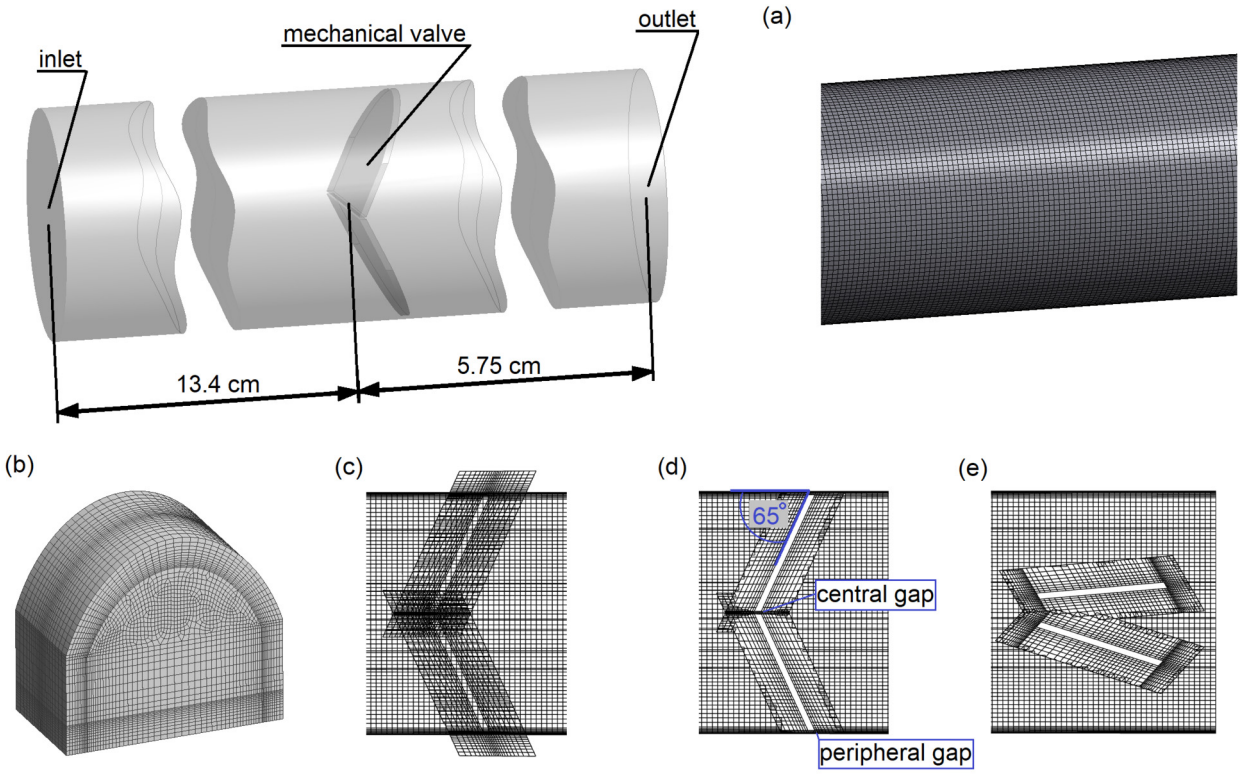

Fig. 1. Numerical mesh prepared for the overset approach: **(a)** - geometry and fragment of the background mesh, **(b)** - component mesh, **(c)**, **(d)**, **(e)** - cross-sections through the joined background and component meshes: **(c)** - before matching process, **(d)** - after matching process (fully closed state), **(e)** - after matching process (fully opened state). The mechanical valve leaflets position changes because of the transient fluid flow, from the closed **(d)** to opened **(e)** state, and even in the fully closed position, small flow gaps are present: central gap and peripheral gap.

technology allows to perform calculations on the overlapping meshes, i.e. the stationary background mesh and component mesh, or to decompose a domain into multiple discretized bodies coupled together. The interpolation is performed between the meshes, to transfer the information between them [46–51]. Four kinds of cells are present after the process of coupling meshes together. The *dead cells* are those that fall outside the domain, and they were present in this investigation, especially when the valve was almost closed or fully closed, because the range of the structural mesh leaflet surrounding was preferred to be wider than determined by the vessel scope. The computation process is performed on the *solve cells*. The interpolation is realized between the *donor cells* and the *receptor cells*, where the latter receives the data from the former.

In this research, the overset method was also used to update the geometry and mesh due to the leaflets movement. The overset technique significantly improved the computational stability and solver convergence, compared to the case of dynamic mesh usage instead. Moreover, it enabled the hexahedral structural mesh creation and preservation during body movement in the most part of the two individual leaflet surroundings and in the background as well. The additional advantage of the overset meshing is the limitation of the solver wall clock time, because this utility is less consuming than smoothing or remeshing, and eliminates the negative cell volume error. This error will stop the solution process. Furthermore, the dynamic mesh could deteriorate the cells quality, especially by increasing skewness parameter, when the rotations per timestep are high. Taking into account the above remarks, in this research, the overset mesh was prepared and used for the 6DOF model and the analysis of the results. However, dynamic mesh was used additionally to compare the results with different moving mesh approaches (Section 7.6).

4. Numerical model

FSI modeling of the artificial bileaflet valve involves calculation of the leaflet rotations and deformations. The material constant describing body elasticity, i.e. susceptibility on deformations, is Young's modulus. The Young's modulus of the valve leaflets, which are mainly created of pyrolytic carbon, is on the level of 29.4 GPa [52] and is about twenty thousands times higher than the modulus of the elastic blood walls. Because of that, the bileaflet valve does undergo substantial deformations influencing results and the rigid body assumption is commonly applied [53]. In the presented work, the rigid body motion solver discussed later, was implemented into the Ansys® Fluent solution procedure using set of UDFs. The commercial Fluent software has already six degrees of freedom solver available, however, its usage for the problems involving fast rotations of the body whose intertial moment is on the level of $10^{-9} \div 10^{-7} kg \cdot m^2$ fell short due to several reasons. Firstly, serious problems were experienced with achieving convergence and build-in stabilization mechanisms, as changing stabilization factors and implicit updates did not help. Due to the lack of access to the source code, any further solver manipulation was not achievable. Secondly, it was not clear which moment of inertia should be imputed, namely, if the global or local coordinates should be considered. It was also not known whether both the pressure and viscous forces were applied to calculate the motion. Third, there were problems with blocking motion when the leaflets achieved the maximum or minimum allowable angle. Ansys enabled the possibility of wide customization using User-Defined Functions (UDFs) and it was decided to implement in-house rigid body motion model. This let to get rid of any insecurities and allowed the additional manipulation, debugging, and results postprocessing. The results of the implemented model were compared with the build of the 6DOF solver, using several other simpler-to-converge cases, and any substantial differences were not observed. The in-house implementation of the

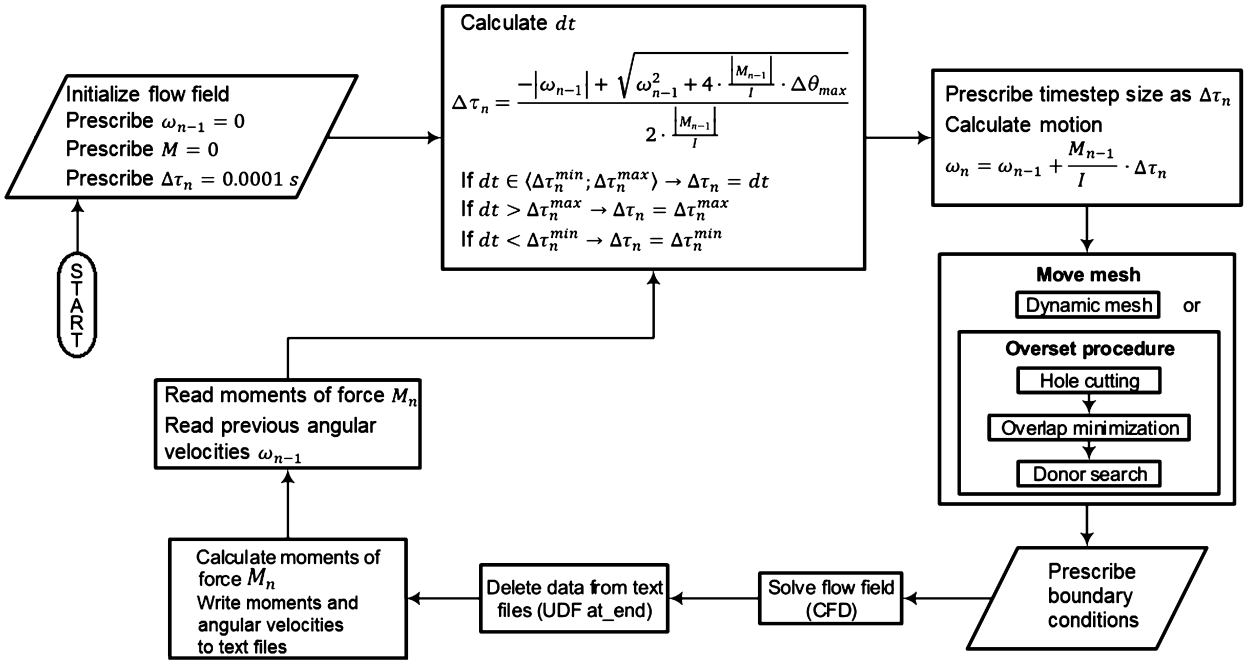

Fig. 2. Flowchart of the six degrees of freedom model with adaptive timestep size, implemented into the Fluent standalone solver, for determination of the transient valve leaflets angular positions. The valve leaflets are assumed as rigid and can only rotate around the axis, when their angular positions are in between the closed and opened state, presented in Fig. 1. The leaflets rotate by the effect of the forces exerted by the flowing fluid.

solver into a commercial software was presented, to overcome issues and possibly accomodate its usage among researchers, moreover presenting the detailed equations and flowcharts makes it possible to implement the model within the open source packages, as e.g. openFOAM, OOMPH-lib or Fenics. The 6DOF model applicability is found in rigid structures, such as one-, two- or three-leaflet artificial valves, where the forces exerted by the fluid are retrieved from the fluid solver and then this solver calculates the leaflets rotational velocity, using equations including the leaflet inertial moment. It is necessary to implement some approach for the moving mesh, as a dynamic or overset mesh, to absorb the motion in a domain.

In the classical rigid body motion theory, the motion of the body is decomposed into translation along three directions and rotations around three axes [54]. To calculate every motion component properly, two different coordinate systems are used: the global (inertial), which is fixed, and the body (local) coordinate system. The origin of the body coordinate system is generally placed at the rigid body's center of gravity. In considered case, where only one degree of freedom is allowed (1 rotation), the origin is in the center of the axis of rotation.

The rotational motions are calculated in the local coordinate system. The body's momentum of momentum is defined

$$\mathbf{L_B} = I \cdot \omega_B \tag{1}$$

where I is the inertia tensor, ω_B is the rigid body angular velocity vector in the local coordinate system. The momentum theorem

$$\frac{\mathrm{d}\mathbf{L_B}}{\mathrm{d}\tau} = \mathbf{M_B} \tag{2}$$

is applied to the body coordinate system. Finally, the governing equation for angular motion is as follows [54]:

$$I \cdot \frac{\mathrm{d}\vec{\omega}_B}{\mathrm{d}\tau} + \vec{\omega}_B \times \left(I \cdot \vec{\omega}_B\right) = \mathbf{M_B} \tag{3}$$

The transformation matrix T is used to transform the moments from the inertial coordinate to local coordinates with equation $\mathbf{M_B} = T \cdot \mathbf{M_I}$.

The flowchart in Fig. 2 presents the implementation of the 6DOF model in Fluent. The UDFs and Fluent journal files were used for this purpose.

At the beginning of the computation, the flow field is initialized, as well as the variables used in model. Then, the timestep size for the solver is determined. Although the Courant–Friedrichs–Lewy condition is widely used to determine the proper timestep size for the given flow field and spatial discretization, such a method will not manage to adjust the timestep size to the velocity of the moving body. Therefore the dynamic timestep size was implemented, for several reasons. It was intended to avoid the orphan cells (in case of overset) and negative cell volumes (in case of dynamic mesh), which are present when too much rotation is performed in a single timestep. This could also deteriorate the mesh quality. In addition, the better solution accuracy is expected when the timestep is smaller than when the angular velocity is higher. Moreover, this leads simultaneously to optimize the solution time. The dynamic timestep size was realized using UDF `define_deltat`. The value is calculated using equation:

$$\Delta\tau_n = \frac{-|\omega_{n-1}| + \sqrt{\omega_{n-1}^2 + 4 \cdot \frac{|M_{n-1}|}{I} \cdot \Delta\theta_{max}}}{2 \cdot \frac{|M_{n-1}|}{I}} \tag{4}$$

The derivation of the above formula is as follows: the maximum allowable increment of the angle per timestep $\Delta\theta_{max}$ is specified as the constant value. Then, a set of equations for the n-th timestep was prepared:

$$\begin{aligned} \Delta\theta_{max} &= |\theta_n - \theta_{n-1}| \\ \Delta\theta_{max} &= |\omega_n \cdot \Delta\tau_n| \\ \omega_n &= \omega_{n-1} + \frac{M_{n-1}}{I} \cdot \Delta\tau_n \end{aligned} \tag{5}$$

Transforming the set of equations (5) lead to the quadratic function of $\Delta\tau_n$:

$$\frac{M_{n-1}}{I} \cdot \Delta\tau_n^2 + |\omega_{n-1}| \cdot \Delta\tau_n - \Delta\theta_{max} = 0 \tag{6}$$

Solving this function gives two roots, where only one (presented by equation (4)) represents non-negative values, thus only this root could

be chosen as a solution, because the time increment must represent a positive value. As two valve leaflets are present, two different values of $\Delta\tau_n$ are obtained, where the lower value is taken to adjust the time discretization of the leaflet, that is rotating faster. It was also necessary to define the maximum allowed timestep size equal to 0.001 s, to avoid setting excessively large values of dt when the valve is stationary. The minimum timestep set as $5 \cdot 10^{-6}$ s was specified to restrict the timestep in the case if the formulas give unreasonably low values. After prescribing the timestep size to the solver, the angular motion is calculated with the recursive formula:

$$\omega_n = \omega_{n-1} + \frac{M_{n-1}}{I} \cdot \Delta\tau_n \tag{7}$$

where M_{n-1} is the force moment in step $n-1$. This formula comes from the differential equation for the angular motion towards a single axis, and solving it using Euler method:

$$M = I \cdot \frac{d\omega}{d\tau} \quad -> \quad d\omega = \frac{M}{I} d\tau \tag{8}$$

The initial condition was set as $\omega(\tau = 0) = 0\ rad/s$. The adaptive timestepping for the Euler method is applied using the derived equation (4).

The force moment M_{n-1} is calculated based on the pressure (P) and wall shear stress (WSS) field from the previous timestep. Firstly, the pressure and WSS are integrated over the leaflet wall. Then, based on the force translation theorem, the resultant force is obtained, and it is transformed to the force moment based on the vector distance from the center of rotation:

$$M_{n-1} = M^{p}_{n-1} + M^{WSS}_{n-1} = \sum_{i=0}^{n_b} (P_i A_i \vec{k}_i) \times r_i + \sum_{i=0}^{n_b} (WSS_i A_i \vec{k}_i) \times r_i \tag{9}$$

where n_b represents the number of the faces on the leaflet boundary, P_i and WSS_i are the pressure and wall shear stress exerted on the leaflet at i-th mesh face, with its vector indicated as k_i; A_i is the area of the i-th leaflet mesh face and r_i is the distance of the mesh face from the rotational axis.

Finally, when the angular velocities are calculated, the leaflets are moving in the fluid domain using macro `define_cg_motion` and this motion is absorbed by the moving mesh module. The model works using text files, created by Fluent journals and UDFs. Part of these files have to be empty at the end of the step, which is realized by UDF `define_at_end`.

During the first 80 timesteps, the angular velocity is linearly ramped against the function of timestep number: $\omega_n = \omega_n \cdot (0.0125 \cdot n\_time)$, where n_time is the integer number of timestep. This way, starting from the 80^{th} timestep, the total value of angular velocity determined by Eq. (7) is imposed on the valve leaflet. The ramping was added to start the rotation more slowly, only at the beginning of the computation, when the velocity field is not yet fully developed, thus harder to resolve. Small number of large force moments higher by orders of magnitude was experienced, in this case they were treated as gross errors by adding to the UDFs conditional statements that discard these kinds of values. As the leaflets can rotate in the specified angular range, an additional module was added that suppresses the rotation, when the maximum or minimum allowable angle is achieved. The rotation is unblocked, when the force moment takes the opposite sign, which promotes the rotation in the opposite direction.

For the better computational stability at the beginning of the first cycle, the computation starts from the valve at the slightly opened state - with the leaflets rotated by 20° from the closed position. At this state, the flow field is less impacted by the valve presence, compared to the closed state, therefore such initial position allowed the faster solver convergence during the first calculated heart cycle. The angular state at any moment is not known a priori, so several heart cycles were calculated for every set of boundary conditions, until fully repeatable results were achieved.

5. The governing equations

The finite-volume solver (Ansys Fluent) calculates the flow field based on solving the set of partial differential equations ((10), (11)), formed for the unsteady flow as follows:

$$\frac{\partial \rho}{\partial t} + \nabla \cdot \left(\rho \overline{\mathbf{u}}\right) = 0 \tag{10}$$

$$\frac{\partial}{\partial t}\left(\rho \overline{\mathbf{u}}\right) + \nabla \cdot \left(\rho \overline{\mathbf{u}}\overline{\mathbf{u}}\right) = -\nabla p + \nabla \cdot \left(\overline{\overline{\tau}}\right) \tag{11}$$

where ρ is the fluid density, t is the time and $\mathbf{u}$ is the velocity vector [55,56]. The stress tensor $\overline{\tau}$ is defined as

$$\overline{\overline{\tau}} = \eta \left[\left(\nabla \mathbf{u} + \nabla \mathbf{u}^T\right) - \frac{2}{3} \nabla \cdot \mathbf{u} I \right] \tag{12}$$

where I is the unit tensor, and the term on the right side of the bracket is the effect of volume dilation [55] For the constant density $\frac{\partial \rho}{\partial t} = 0$ and $\frac{2}{3} \nabla \cdot \mathbf{u} I = 0$.

The dimensionless quantity that characterizes the flow state is the Reynolds number [55]. It is the ratio of inertial to viscous forces and is defined by $Re = \rho u d / \mu$, where ρ is the fluid density, u is the velocity, d stands for the characteristic dimension (for pipe, diameter) and μ is the dynamic viscosity. According to different sources [55–57], the flow could be assumed as laminar when the Reynolds number does not exceed the maximum value from 2100 to 2300. Therefore, the arterial flow is mainly laminar, except the brief period immediately post-systole in the ascending aorta, when the instantaneous Re value falls between 4.000:5.000 [57,58]. Research [59] indicated that the shear layer instability lead to the turbulence transition and the resolving spatial resolution of 100 μm is necessary to assess the possible blood cell damage and platelet activation. The impact of different design characteristics on the flow and platelet phenomena is described in [60]. Turbulence and flow eddies, coagulability and the presence of non-endothelialised surfaces are the factors that induce thrombosis [61,62]. In the test rig measurement, the maximum Reynolds number was on the level of 16.000 for some short time intervals. The described factors suggest the necessity of applying some approaches for turbulence modeling. Thus, the Reynolds-averaged Navier–Stokes (RANS) turbulence $k-\epsilon$ model was utilized, as a fast RANS model recommended to the locally transitional flows with the boundary layer separation.

The prepared model can operate with any possible boundary condition applied. In this research, to properly represent the mass flow and pressure levels, the inlet velocity and outlet pressure boundary conditions were used, as presented in Fig. 5. The time-varying values were simulated using measurement data, via the usage of several approximation polynomials for each measurement set. The use of multiple polynomials allowed a better representation of the measurement data, where coefficient of determination was on the level of 99%. For the walls, no-slip BC was established, which means that the fluid at the surface of the wall moves with the same velocity as the adjacent wall. The solving process was initialized with the 0 values of the computed variables within the geometry scope, except for the inlet and the outlet surfaces, where the velocity and pressure values came from the boundary conditions. The substance used in model is water, as in the test rig. The properties were set: density 998.2 kg/m^3 and dynamic viscosity 0.001003 kg/(m·s). The details concerning application of the non-Newtonian viscosity model for the blood can be found in [63].

6. Laboratory test rig and measurements

During the experimental investigations at in-house test rig illustrated in 3, a bileaflet artificial heart valve was tested. The polycarbonate valve holder is connected to the pulsating blood pump (Harvard Apparatus®). The pump has the possibility to change heart rate and the percentage difference between systolic and diastolic stroke volume, as well as the size of the ejection chamber. Electromagnetic flow meter, Enderess+Hauser,

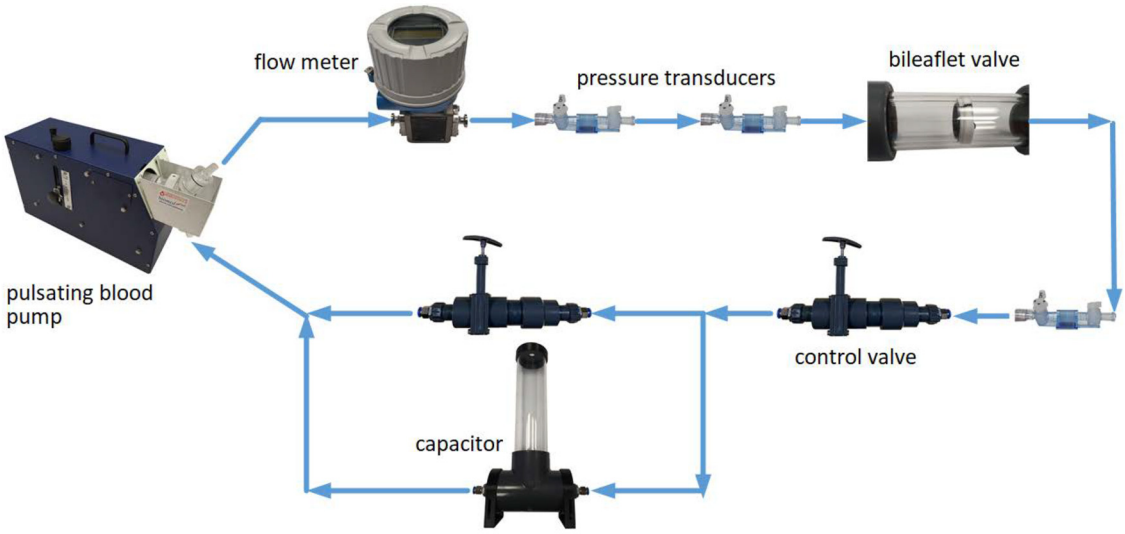

Fig. 3. Configuration of the laboratory test rig, prepared for the numerical model validation and determination of the model constant. The pulsating fluid flow was induced by the peristaltic pump. The measured quantities are: mass flow, pressure before and after the valve prosthesis, and the valve motion is recorded by the fast camera.

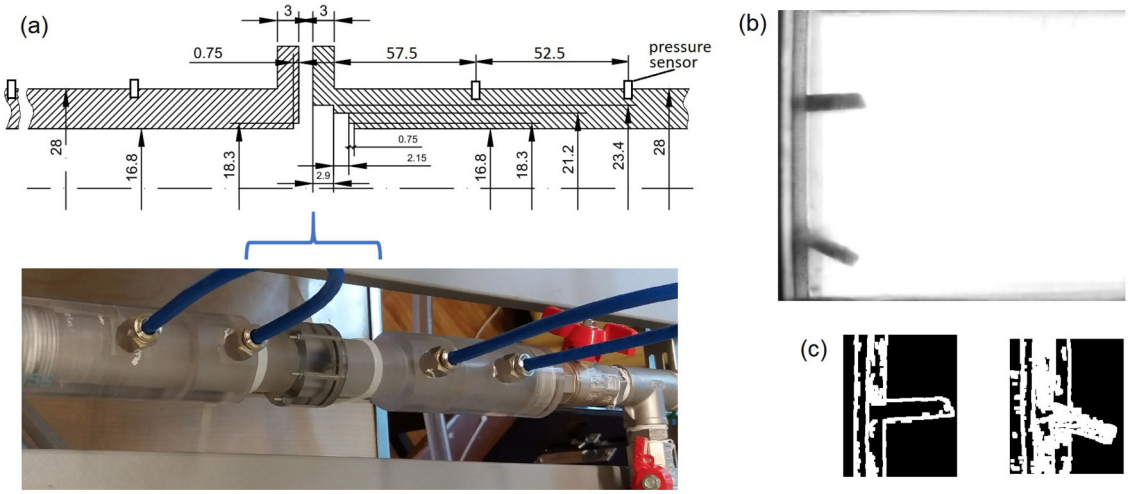

Fig. 4. Aortic valve prosthesis installed in the laboratory setup: **(a)** - designed aortic valve holder with marked dimensions; **(b)** - fast camera image; **(c)** - fragments of the upper and lower leaflets regions extracted from the camera image, after OpenCV processing.

Promag 100 [64] was used to measure flow rate through investigated valve. Selected flow meter does not generate pressure loss and thanks of the frequency output it was possible to acquire flow profile with desired accuracy, to use it for further numerical model setup.

For measurement of the pressure profile during the pump cycle, four fast static pressure sensors (APT 300 – sapling rate: 1 kHz) were used as shown in Fig. 4(a). An additional pressure sensor was placed 26 cm before the valve. Information collected from these locations as well as from the flow meter were necessary for a proper initialization of the numerical simulations.

To capture the movements of the valve leaflets, a high-speed camera VEO 710L [65] was equipped with a NIKKOR 200 mm F/4.0 MACRO lens. This configuration allowed the tracking of leaflets movement at a resolution of 1280 x 800 pixels and a rate of 9,800 frames per second. To ensure sufficient illumination for the camera, a back-light (LED Phlox HSC Phantom 10 x 10 cm) was used with a luminance of ≥130.000 cd/m^2, uniformity of ≥ 95%, and light temperature of 5.700 K. An example of recorded image is shown in Fig. 4B.

The installation was controlled by an in-house application written in National Instruments LabVIEW (National Instruments Corp., USA) [66] to synchronize the measurements with the pump cycle and camera. To capture the flow rate through the rig, LabVIEW FPGA was used, for efficient and effective control of the complex systems by application of a highly integrated development environment. All experimental results were stored in ASCI format for future processing.

In the laboratory test-rig, the vertical tube capacitors were used to maintain the constant pressure levels in the measurement system. They were used as the representation of the last part of the circulatory system of a human being [67,68]. In terms of the human body, they account for the interaction between the stroke volume and the compliance of the aorta and large elastic arteries (Windkessel vessels) and the resistance of the smaller arteries and arterioles. In conclusion, the distensibility of the aorta and large elastic arteries is therefore analogous to the capacitors used.

Measurements were performed for five different conditions, resulting from different heart pump settings by adjustment of pump rates, stroke volume and the stroke volume division between the systole and diastole, as described in Table 1. Thus, different velocities and pressure levels were achieved, as well as the cycle times, as shown in Fig. 5. Several polynomials per dataset, fitted using least-squares method, were used to predict the values between the measurement points, to use it as a boundary contidion in the solver. The numerical model was tested and

Table 1
Pulsating blood pump settings applied for the measurement datasets.

Dataset no.	%systole: %diastole %: %	Pump rate RPM	Volume per stroke cm^3	Resulting cycle time s
1^{st}	30:70	50	80	1.20
2^{nd}	30:70	60	80	1.02
3^{rd}	30:70	70	80	0.84
4^{th}	35:65	60	80	1.02
5^{th}	40:60	60	80	0.98

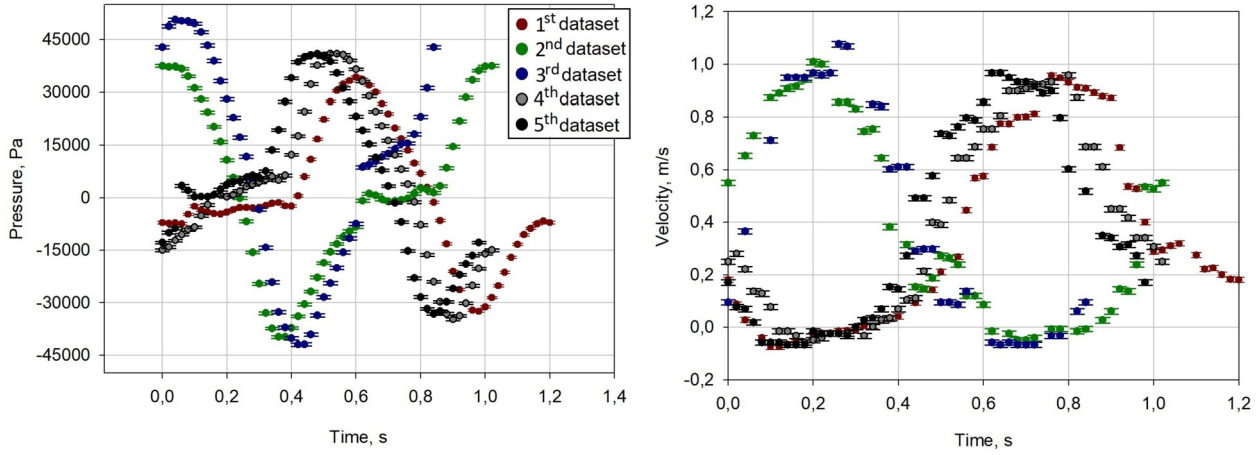

Fig. 5. Measurement data provided for the numerical model boundary conditions, presented for five datasets. At the inlet of the domain, the velocity profile is imposed, whereas at the outlet the pressure boundary condition is assigned. The polynomial time functions were prepared, to determine the velocity and pressure values for the every timestep in the solver.

validated on the basis of every dataset. The model constant, moment of inertia, was calibrated based on 5^{th} dataset, then using four remaining ones the calculations were performed and validated, to assess its reliability in different flow conditions. The choice of 5^{th} dataset for calibration was based on the pump settings closest to the average applied.

6.1. Computer vision image analysis for determining leaflet angles

The fast camera greyscale images registered during the test rig measurements were used to validate the numerical model results in terms of the leaflets angular motion. Thus, these images have to be processed into the values of the leaflets angle. The visual and manual inspection is highly inefficient, time-consuming, non-replicable and inaccurate. Thus, the procedure for angle determination was created in Python OpenCV environment [42]. In the prepared algorithm, it was necessary to transform the parts of greyscale images into binary format, where the number *0* is referred to black, and number *1* to white color. The typical conversion to binary itself, as in previous work [69] worked well, however, it was chosen the Canny operation over the binary conversion [70]. The reason is that this allowed for the better identification of the leaflets edges. The Canny algorithm is the edge detection technique, consisting of Gauss filtering, gradient calculation, non-maximum suppression, double thresholding, checking the edges and connecting the edges [71,72]. The Canny threshold values $THR_{min} = 25$ and $THR_{max} = 50$ worked well in this study.

Developed algorithm for automatic determination of leaflet angle works as follows. At first, the fast camera image is loaded, and the fragments, where the upper valve leaflet is visible (in previously defined coordinates) is cutted. Similar procedure is repeated for the lower leaflet. Described procedure is done for all the pictures from the fast camera folder. Afterwards, the cutted images are loaded and the Canny operation is performed, to extract the leaflet edges and make them white, for easier identification, as presented in Fig. 4. Then, these edges are thickened with *dilate* operation, to facilitate the processing of images that may be blurred. The procedure is searching for the first white pixel, starting from the upper right corner (for upper leaflet) and lower right corner (for lower leaflet). This way, the coordinates of ending of both leaflets are found. The last step is the calculation of the arcus tangens of the slope of straight line, which is created between two points: ending of the leaflet and its center of rotation. This way the angles of both leaflets are determined. The centers of rotation were found by overlaying several images, where the valve was in different positions. The leaflet edges were extended, to find the point where extensions intersect each other, then the point coordinates were read out.

7. Results and discussion

7.1. Dynamic timestep size sensitivity analysis

The timestep size for time intervals where leaflets are moving, is calculated using equation (4). Thus, excessive mesh distortion is avoided, by time discretization adaptation. For stationary leaflets, fixed value of $\Delta\tau_n = 0.001\ s$ was applied, as in previous work [73]. The model constant in equation (4), $\Delta\theta_{max}$, describes the maximum allowable angular displacement per single timestep, and affect directly the computational time. The timestep size sensitivity analysis was performed on fifth dataset, by using different values of $\Delta\theta_{max}$. This was done to check, how the number of timesteps increases by lowering this value, to check whether it impact onto numerical model results and also to assess the moving mesh operation. The results are presented in Fig. 6 and Table 2. The number of timesteps per heart cycle decreases rapidly up to the value of $\Delta\theta_{max} = 0.2°/ts$, then the change becomes inconsiderable. After increasing the allowable angular displecement to 0.5 degree per timestep, the model could not be resolved due to the orphan cells. The computational saving was calculated, comparing the $\Delta\tau$ per cycle, with the number of timesteps which will be necessary to ensure applied $\Delta\theta_{max}$ with the constant timestep:

$$solv_{red} = \frac{n_{\Delta\tau\_dyn}}{n_{\Delta\tau\_const}} \cdot 100\% = \frac{n_{\Delta\tau\_dyn}}{\frac{cycle\ time}{\Delta\tau_{min}}} \cdot 100\% \tag{13}$$

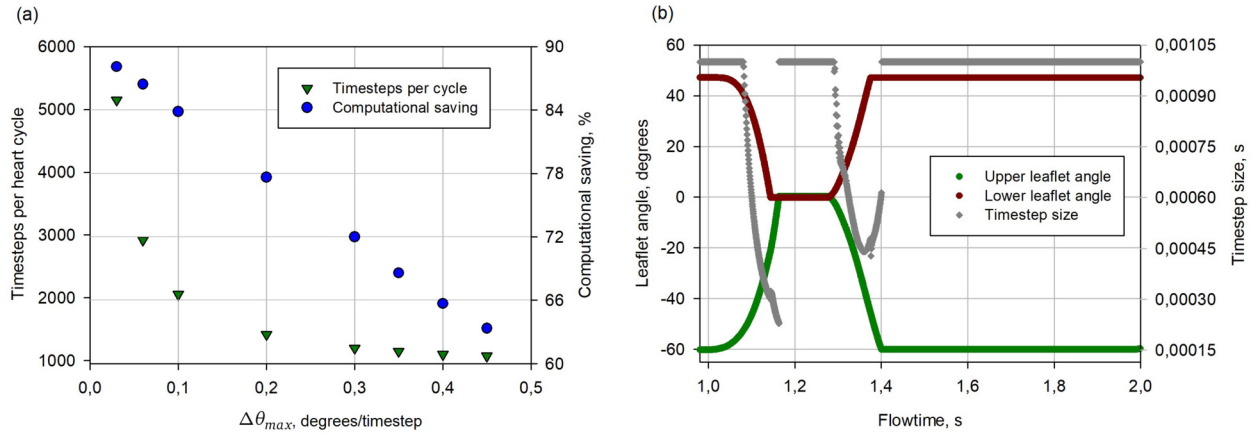

Fig. 6. (a): Timestep size sensitivity analysis, based on changing the model constant $\Delta\theta_{max}$. The value $\Delta\theta_{max} = 0.3°/ts$ was selected, as the further increasing allowed rotation per single timestep does not decrease substantially solving time, and may cause the moving mesh or solver convergence failure; **(b)**: results obtained for the selected value $\Delta\theta_{max} = 0.3°/ts$ - leaflets angle time profiles with the variable timestep size.

where $solv_{red}$ is the solving time reduction, $n_{\Delta\tau\_dyn}$ - number of timesteps resulted from applied time discretization methodology, $n_{\Delta\tau\_const}$ - number of timesteps for constant time discretization, $\Delta\tau_{min}$ - minimum timestep size (which occurred during the fastest angular velocity). The decrease in the number of time steps needed to solve the model, potentially decreases the computational time. The calculation time for two heart cycles was equal approximately 48 h, using six 3.6 GHz IntelCore i7-11700 K cores.

The computational saving is highest for the lowest angular displacement per timestep and decreases linearly with increasing $\Delta\theta_{max}$. The leaflets' angular time variations, as well as pressure values, were compared for different $\Delta\theta_{max}$. The conclusion was made, that for the considered time discretizations, the results are independent. Possibly, applying the highest maximum timestep, some flow field characteristics would differ, however this was not necessary due to time-efficient time discretization.

Considering the described remarks, the model constant of $\Delta\theta_{max} = 0.3°/ts$ was used, mainly due to inconsiderable timesteps reduction with higher $\Delta\theta_{max}$, and to avoid eventual orphan cells. Described time discretization model enables the faster computations and lowers the hardware requirements, making it more applicable for the clinical purposes.

The final leaflet time angle profile with plotted timestep size is presented in Fig. 6. The angle of 0° is referred to the closed state. As observed, the value depends on the angular velocity (i.e., angle curve slope), changing smoothly during valve motion.

7.2. Moment of inertia multivariant analysis

The usage of the 6DOF model in this case could be restricted to only one rotation around the z axis. The proper momentum of inertia has to be calculated. This quantity determines how large the rotational force should be, to achieve specified angular acceleration around the rotational axis [74]. Only one from the nine inertial tensor components is here demanded: $I = I_{zz} = \int_m \left(x^2 + y^2\right) dm$, where dm is an infinitesimal mass of the body. According to this equation, the value depends on the chosen axis, body mass and its distribution.

Several different ways are available to determine the moment of inertia. Sometimes the value can be measured using the rotary disc. For the simpler geometrical features, the analytical formulas are possible. For example, the valve leaflet could be estimated as the disc half with radius R, whose value calculated against the half disc edge equals $I = 0.25 \cdot m \cdot R^2$. As the inertial moment is the additive property, the composite system is the sum of the moments of inertia of its component subsystems, only if the same axis is considered. Thus, the computer software products can be used for any complex geometrical features, to calculate the momentum of inertia, virtually dividing the geometry into simpler shapes. Due to more complex leaflets' geometrical character and rotational axis location, the SpaceClaim software mass tools were utilized [75]. This way the inertial moment value divided by the density could be found, with the rotational axis coincide with the center of gravity. This is called principal moment [mm^2] [45,74]. To ascertain, that the used software calculates proper values, several cases where the analytical solutions are available were prepared and almost the same results were obtained as analytical. Then, the mean leaflet density was calculated. Is made from pyrolytic carbon ($\rho = 1940\ kg/m^3$) and coated by tungsten ($\rho = 19300\ kg/m^3$) in 20% by weight [76,77]. The below set of equations:

$$\begin{aligned} m_t &= 0.2 \cdot m_l \\ m_l = m_W + m_C &= V_W \cdot \rho_W + V_C \cdot \rho_C \\ V_l &= V_W + V_C \end{aligned} \tag{14}$$

where: m - mass, V - volume, ρ - density, C - pyrolytic carbon, W - tungsten, l - leaflet, let to calculate the mean density of the leaflet, equal $\rho_l = m_l/V_l = 2365.6$ kg/m^3. Then the value of principle moment from SpaceClaim was multiplied by the calculated density and the principal inertial moment was obtained: $I_0 = 2.62 \cdot 10^{-9}$ kg·m^2. However, it was determined that the rotational axis is in the position located 15% of the valve radius from the vessel centerline (Fig. 1D, E). Thus, the Steiner's law for parallel axes was used to transform the calculated moment to proper axis [78]:

$$I_{geom} = I_0 + m \cdot a^2 \tag{15}$$

where I_0 is the moment of inertia with respect to the axis passing through the center of mass, m is the mass of the body and a is the distance between the two axes. Finally, the value $I_{geom} = 3.5331 \cdot 10^{-9}\ kg \cdot m^2$ was obtained. However, the valve motion is influenced by factors slowing down the motion, extending beyond the rotational inertia, and not possible to calculate or easily measure. These factors are, e.g., the friction of the mechanism, small particle deposition, impurities in the laboratory test rig, water settling on the valve, and leaflets mass distribution nonuniformity. Moreover, it was noticed that different values of I were used in other works, depending on the inner diameter size and assumed or calculated leaflet material density (compare: [13] $8.75 \cdot 10^{-9}\ kg \cdot m^2$, [79] $7.947 \cdot 10^{-9}\ kg \cdot m^2$, [80] $3.99 \cdot 10^{-9}\ kg \cdot m^2$, [81] $6.95 \cdot 10^{-9}\ kg \cdot m^2$). Therefore, faster rotations were determined than observed in the test rig. To find the proper I constant that includes every factor that influence the motion, the calculated value was magnified with different multipliers $n > 1$: $I = n \cdot I_{geom}$ until the differences between the measurement data and the numerical model were minimized. To assess these differences, the function **F** - equation (16) was prepared.

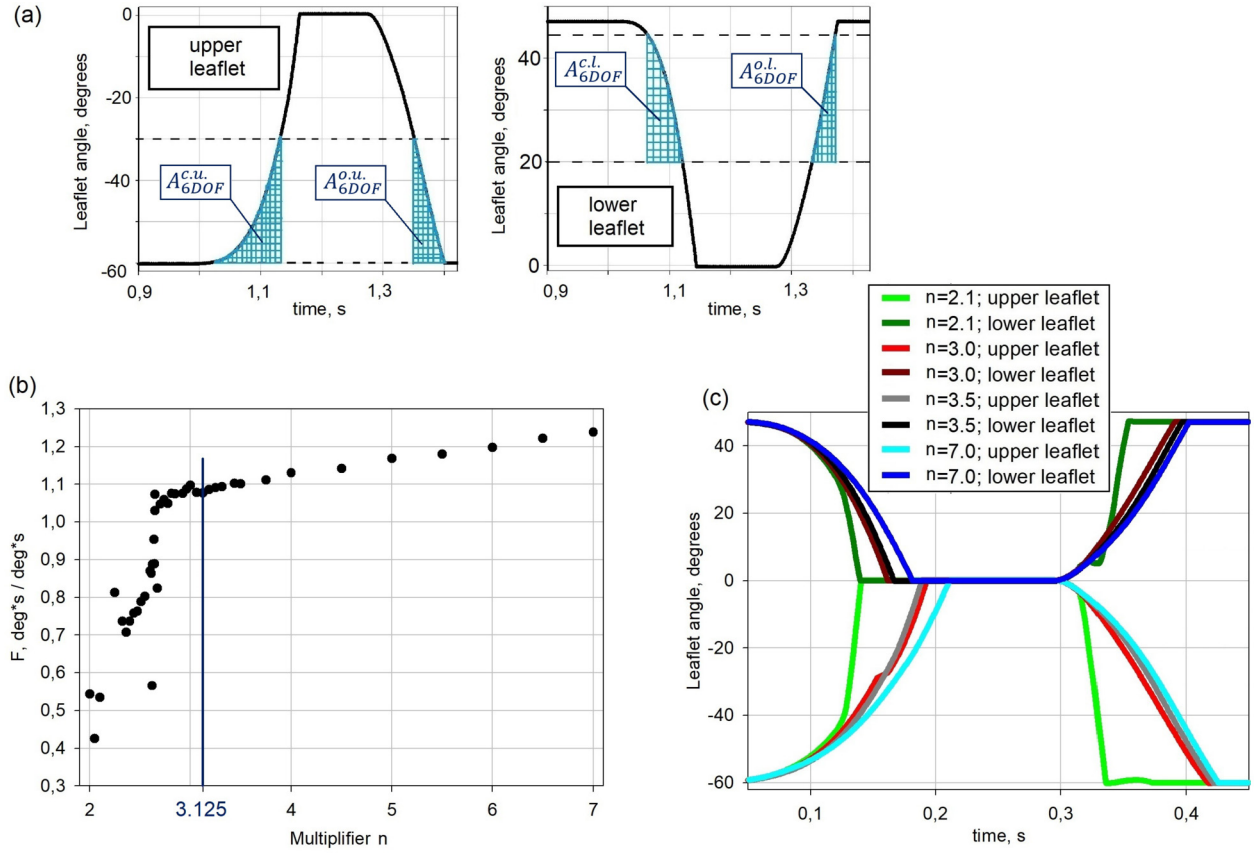

Fig. 7. Multivariant analysis for the model constant - moment of inertia I: **(a)** - areas under the curves obtained for a given I value; the total area $A_{6DOF}(n)$ (dashed blue surface) was used then in function F - equation (16); **(b)** - function F values obtained for different multiplifiers n of the inertial moment. The value of $F = 1.0$ means the same area under the curve obtained from the mathematical model and the measurement. The multiplifier value of $n = 3.125$ was chosen for the analysis; **(c)** - leaflets angle time courses for different n values.

Table 2
Indicators obtained from the dynamic timestep size sensitivity analysis, related to the model solving time. The analysis lead to choose the model constant value of $\Delta\theta_{max} = 0.3°/ts$, as the compromise between the computational demandings and the possibility of solver failure.

No.	$\Delta\theta_{max}$, deg/ts	$\Delta\tau$ per cycle, ts/cycle	$\Delta\tau_{min}$, s	$\frac{cycle\ time}{\Delta\tau_{min}}$, -	computational saving, %
1	0.03	5 149	0.000 023	43 257	88%
2	0.06	2 916	0.000 046	21 493	86%
3	0.10	2 054	0.000 077	12 710	84%
4	0.20	1 417	0.000 155	6 335	78%
5	0.30	1 198	0.000 229	4 278	72%
6	0.35	1 148	0.000 268	3 653	69%
7	0.40	1 100	0.000 306	3 205	66%
7	0.45	1 072	0.000 335	2 924	63%
9	0.50	unconverged results			

It was based on calculating the area under the leaflet angle courses, for the angles that are visible in the fast camera field of view, as presented in Fig. 7(a). The base area A_{meas} was calculated using the fast camera data.

$$F(n) = \frac{A_{6DOF}(n)}{A_{meas}} = \frac{A^{c.u.}_{6DOF}(n) + A^{o.u.}_{6DOF}(n) + A^{c.l.}_{6DOF}(n) + A^{o.l.}_{6DOF}(n)}{A^{c.u.}_{meas} + A^{o.u.}_{meas} + A^{c.l.}_{meas} + A^{o.l.}_{meas}} \tag{16}$$

where $c.$ - closing, $o.$ - opening, $u.$ - upper leaflet, $l.$ - lower leaflet

By considering the areas under time angle course, it was possible to analyze the model differences in the motion in the whole spectrum that leaflets were visible at camera. If the function was based, e.g., on the times between certain angular states, it would omit the motion profile.

Calculation of 43 cases with different inertia multipliers in the scope $2 \le n \le 7$ was performed. To obtain the results of the model as close to measurement as possible, the multiplier n should be chosen for which function F has value of 1. The results of the multivariate analysis are presented in Fig. 7 - the variance of the function F together with the angle time courses. It was stated that the 6DOf model is quite sensitive in the multiplier scope $2.0 \le n \le 2.7$, then up to the maximum analyzed value of 7 function F changes slowly and linearly. It is also apparent that when the angle time variations are compared - the angular course between $m = 3$ and $m = 7$ differs much less, than between $n = 2$ and $n = 3$. In the multiplier range $< 2.75; 3.5 >$ the results remain almost the same. Thus, the average value in this scope $n = 3.125$ was finally chosen, as the model results are very close to the measurement (F value close to 1.0) and the model is not sensitive to the errors (upper error and lower error) of inertial moment determination:

$$I = n \cdot I_{geom} = 3.125 \cdot 3.5331 \cdot 10^{-9}\ \mathrm{kg \cdot m^2} = 1.1041 \cdot 10^{-8}\ \mathrm{kg \cdot m^2} \tag{17}$$

The multiplier n was chosen based on calculations performed using the fifth dataset. Then, the remaining four datasets were calculated with the same moment of inertia I, where similar results validity should be expected.

When the moment of inertia is changed, the results variability presented in Fig. 7 comes from several reasons. Firstly, the higher inertial moment promotes slower leaflets' angular velocities, which comes straightforward from the equation (7). However, the values of ω do not change linearly with I, as the equations suggest. This comes from obtaining different moments of force M_{i-1}, which results from the changed

angle of incidence. For example, during the closing phase, when the moment of inertia is lowered, the rotation calculated from equation (7) is faster and thus the angular position is nearer to the closed state. Thus, the fluid hits the leaflet more perpendicularly, which promotes higher forces and force moments. This also promotes even faster rotations. The additional factor that impacts the calculated valve motion for the changed inertial moment is the fact that the inflow profile is fixed as a boundary condition. Thus, the inlet velocity profile corresponds to different leaflets' angular positions - when the moment of inertia is changed. This causes the production of other force moment values for the same inlet velocity.

7.3. Valve leaflet motion

As described in Sec. 7.2, the correction of the model constant - inertial moment I - was performed on the fifth dataset. To check the model validity, four other measurement sets with different flow conditions were performed and solved within the prepared 6DOF model using the same corrected I. As the leaflets motion resistance is independent from the flow condition, the same results validity should be present for both calibration set and validation sets. The results are presented in Fig. 8 and Fig. 9. The uncertainties for the error bars were calculated by checking the times for which several angles (maximum visible, medium, minimum visible) are achieved. This was done for at least eight heart cycles, cause this was the minimum number of cycles captured for every dataset on the fast camera. Afterwards, the standard deviations were calculated. It is worth adding here, that very high repeatability of registered leaflets' angle coursed and fluid pressures was achieved.

Figs. 8 and 9 present the validity of calculated leaflets angles for three cycles. As expected, the first heart cycle is not coincident with the validation data, because the proper valve starting position at the beginning of the simulation is unknown, thus it is always necessary to solve more than one cycle. The results for second and third cycle are the same, so calculating of two heart cycles is sufficient to ensure results repeatability.

The simulation results present satisfying validity with the measurement data for every dataset. The level of validity does not differ between the momentum of inertia calibration (5^{th} data) and four remaining sets. Some minor differences in angle courses between the numerical model and measurement are observed for the lower leaflet, however they generally lay within the scope of one standard deviation. Also, very good validity of the opened state time and extrapolated closed state time is observed, and the moments where leaflets starts moving coincide well. One of the probable reason of differences is a sampling time for the inflow measurement equal $0.02s$ resulting from the device abilities. This time is quite large, comparing that the time necessary to turn from the fully closed to fully opened valve state (or reversely) is on the level of $0.1s$. It was stated, that the inflow profile measurement accuracy is more important for the numerical model time angle reliability, than the pressure measurement (see Sec. 7.5). Also, the uncertainty quantification for the model planned for the future work, will assess which parameters play the key role in the model validity [82].

The inertial moment for the 6DOF model was set as the same value, both for the upper and lower leaflet. This may be the reason why the angular courses deviates from the measurement data slightly more for the lower than upper leaflet. Possibly, the factors slowing down the motion, which extend beyond body inertia, such as mechanism friction and suspended deposition impurities are higher in the lower leaflet in the analyzed case. Performing multivariant analyzes of the inertial moment with allowed different multiplier values for both leaflets may let to obtain even better consistence with fast camera data. However, it was not needed as the validity was stated as satisfactory and this will lead to increase the number of cases with a square. Moreover investigating the multivariant analysis for the multipliers dependent on the leaflets' angle, will increase the number of cases even more. Thus, a single constant value for the inertial moment was used.

7.4. Pressure validation

Validation of the pressure values before the valve location is presented in Fig. 10. Comparison between the numerical and experimental pressure results was performed for all datasets presented in Table 1. The numerical results are presented for the second calculated cycle. It was stated that numerical model presents good agreement with the test rig measurement also in terms of the pressure values. Some inconsistency was stated in the moment, when the leaflets are moving (compare Sec. 7.3). This regularity is observed in the every dataset and may be caused both by the measurement and model errors. When the valve is moving, especially with fast angular velocity, the pressure is rapidly changing, thus it may be harder to measure (notice the gross measurement errors) and calculate its value properly. Also, the pressure in the valve vicinity is highly dependent on the leaflets' angular position, thus, even small angular inconsistency with the measurement data may cause visible discrepancies. However, during the most part of the heart cycles, the measured profiles coincide in the scope of error bars.

7.5. Simplified model results

Comparative analysis was performed for the model, where only the velocity time profile is introduced for the boundary condition. The outlet section was elongated by 50 mm and the 0 Pascals gauge pressure boundary condition was prescribed for the outlet. The model was solved for the 3^{rd} and 4^{th} dataset. The conclusion was made that leaflet motion is governed primarily by the inflow boundary condition - the outlet pressure values do not have a substantial impact on the valve motion - Fig. 11. However, when comparing the values of the pressure exerted on the leaflets, it was stated that the model with 0 Pa constant outlet pressure lowers the leaflet pressure by an order of magnitude. Thus, for the reliable estimate of the valve characteristics, it is necessary to also put the information of the outlet pressure profile into the numerical model, besides the inflow profile.

7.6. Results comparison with dynamic mesh approach

The model results involving overset moving mesh method, were compared with other moving mesh approach - dynamic mesh. This demanded creation of new geometry discretization, which final form is shown in Fig. 12. The dynamic mesh was prepared and solved based on 3^{rd} dataset. This technique is based on two modules: remeshing and smoothing. The smoothing method moves the interior mesh nodes to absorb the motion. When the cell quality characteristics extend beyond defined acceptable values, the cells are locally remeshed, preparing a new tetrahedral mesh. To prepare the geometry for this moving mesh approach, the lefleat geometries were subtracted from the pipe geometry. The new discretization for dynamic mesh was prepared based on the element size and the number of boundary layers settings chosen based on the overset mesh sensitivity analysis. Thus, *medium mesh* settings were applied. The modification for this moving mesh approach was preparing the tetrahedral mesh in the valve surrounding, instead of hexahedral swept mesh (Fig. 12). This was done to allow a remeshing process. The hybrid mesh consisted of 1.200.000 mln of mixed tetrahedral+prism elements (valve region) and 0.76 mln of mixed hexahedral+prism elements (remaining parts).

Three different approaches were used here: 1^{st} - remeshing+diffusion smoothing; 2^{nd} - remeshing+spring smoothing; 3^{rd} - remeshing only, where the mesh was used without the boundary prism layer. The dynamic mesh model calibration was primarily setting the maximum and minimum allowable element size, the acceptable cell skewness limit, and the smoothing parameters which depends how far from the

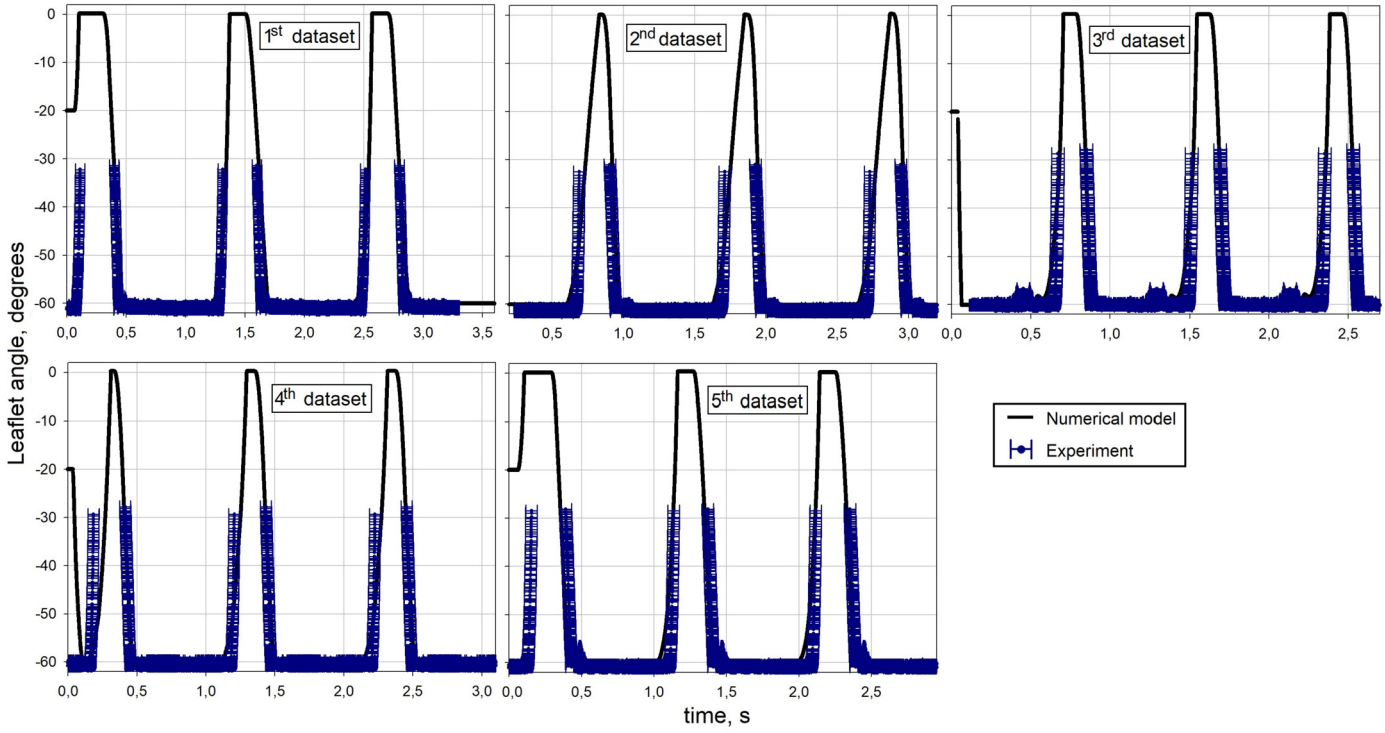

Fig. 8. Numerical model validation, presented for five datasets. The velocity and pressure profiles measured during the experiment were applied to model as a boundary condition, whereas the valve upper leaflet motion, determined by numerical model, is compared with the registered during the experiment. Results are presented for three heart cycles. Angle 0° refers to the closed state, -60° to opened state.

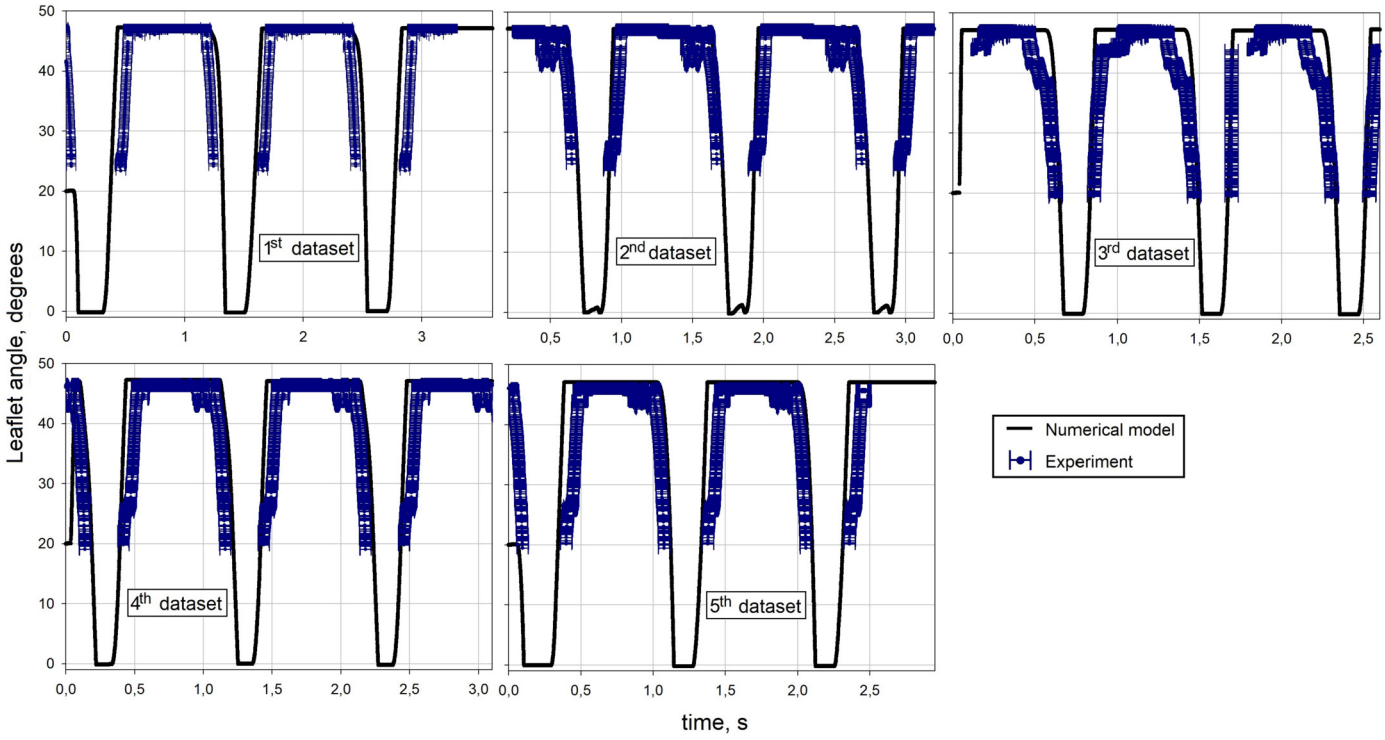

Fig. 9. Numerical model validation, presented for five datasets. The velocity and pressure profiles measured during the experiment were applied to model as a boundary condition, whereas the valve lower leaflet motion, determined by numerical model, is compared with the registered during the experiment. Results are presented for three heart cycles. Angle 0° refers to the closed state, 47° to opened state.

moving body the mesh absorbs its motion. These settings are very case-dependent, where not only geometry but also motion characteristics play its role. Much effort was demanded to prepare proper settings, which allow both to avoid the negative cell volume error and prepare high-quality cells with proper density. Prepared mesh in the valve vicinity is shown in Fig. 13. Outside the geometry region shown in picture, the hexahedral mesh was used as the one prepared for the overset method. Observed smoothing' layer compression and stretching allows

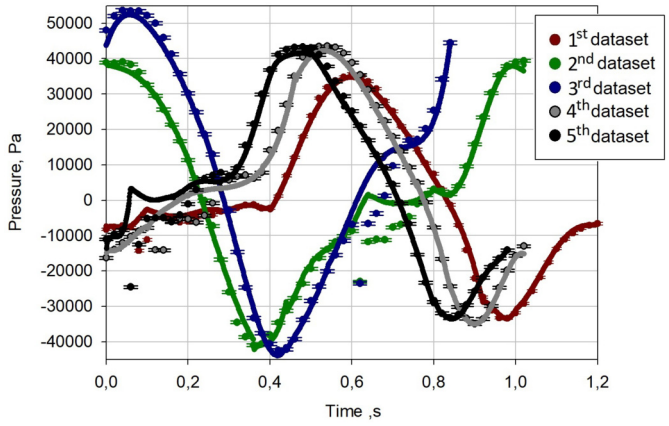

Fig. 10. Validation of the pressure values in section before the valve. Results are presented for five datasets, the measurement is represented by points with errorbars, the numerical results are shown as continuous lines.

to remain good-quality cells, avoid negative cell volumes, and remain proper densification in high gradient regions.

Comparing two approaches, i.e. overset and dynamic mesh, subsequent remarks were done:

- The overset mesh method demands multiple tests on the components and background mesh settings during their creation, whereas preparing discretization for dynamic mesh could be done only once, but different settings in the numerical solver have to be tested for dynamic mesh modules;
- In overset mesh method, a higher maximum leaflet rotation of $\Delta\theta_{\max} = 0.45°/ts$ was allowed to avoid the orphan cells and properly solve the model, where in dynamic mesh the value equal $\Delta\theta_{\max} = 0.3°/ts$ does not allow to avoid negative cell volume error, no matter what settings for mesh motion were applied. Thus, $\Delta\theta_{\max} = 0.075°/ts$ for dynamic mesh timestep size was set and used to solve the model with dynamic mesh method;
- When in the overset approach several orphan cells appeared, the solving process was not affected and residuals represents satisfactory values. In the case of dynamic mesh, the single cell with negative volume causes solving termination with no possibility of restarting the calculation;
- The dynamic mesh method provides conservative calculations, where overset mesh is based on data interpolation between the background and component meshes. However, interpolation is not a problem in the case where a convergent solution is achieved [45];
- Very similar mesh motion patterns were obtained for diffusion and spring smoothing;
- The dynamic mesh method is more error-prone during solving, because during calibration negative cell volume appeared more often than overset' orphan cells. Moreover, it was not possible to calculate three heart cycles using 2^{nd} dynamic mesh approach due to the negative cells, however it was stated that two cycles are sufficient to achieve result repeatability (Sec. 7.3). Furthermore, higher acceptable rotations in the case of overset method entail computational saving (See Fig. 6 and Table 2). Thus, it seems more reasonable to use overset meshing, especially in simulations involving multivariant analyses.
- For a dynamic mesh, the number of elements belonging to the dynamic mesh zone changes with the subsequent timesteps. This change may be substantial, if the settings related to the maximum and minimum allowable element size are not proper. For overset mesh, number of elements remain almost constant - only during the closed valve state some parts of the component bodies exceed the background geometry, which leads to a slight limitation in the solved cell count.
- Very similar results were obtained from both moving mesh methods - see Fig. 14. The differences possibly come from the necessity of producing a new mesh during every timestep, where the motion is present, and the presence of tetrahedral elements in the valve region. In the case of overset method, constant meshes are present, only the donor-receptor pairs changes with motion. The highest differences were noticed in the model where remeshing was used without smoothing (3^{rd} model), however here it was necessary to use a mesh without boundary layer and this is the most possible reason of differences. For the overset, 1^{st} and 2^{nd} dynamic mesh approaches, any visible motion discrepancies are visible only for the upper leaflet during the closing stage.

7.7. CFD results and valve performance indicators

The described numerical model can be used for clinical purposes, as for deciding which artificial valve type, the configuration diameter will work best in the specific patient vasculature. Also, multivariante analyzes can utilize the model and be performed to determine the most appropriate constructions.

In this section, some typical indicators for artificial valves, commonly used in the clinical practice, were described and determined. The results with the overset mesh applied was used for this purpose. Note that some of the quantities will be highly dependent on the patients specific geometry and blood flow conditions, however, the tendency as for the regurgitation gradients and effective orifice area should present regularity for the same prosthesis construction. To assess how the blood flow specifics influence onto indicators, five datasets numerical results were used for the calculation of the indicators. Part of the results described in this section, as wall shear stresses and pressure gradients at leaflets' walls, are not measurable and possible to determine only via CFD calculations.

In this research the *hemodynamic* quantities were determined. The prosthetic valve usage has to be also considered based on their *durability* and *biological response* to the implant [76,83]. The former aspect is related to the structural mechanics and material properties, which influence the susceptibility of the leaflets and housing to erosion, resulting from the cavitation caused from negative pressure transients [76]. The latter will be investigated in future authors work by implementation of hemolysis models, as well as mass transport analysis [84,85].

The artificial valve should not disturb the proper functioning of the cardiac system. Thus, the pressure gradient across the valve should be as small as possible. Larger pressure gradient values may indicate a negative influence on the cardiac output, inhibiting pumping of the proper blood amount and more heart workload [76].

The pressure drop was calculated between two points located on the centerline, 3.5 mm before the valve and 3.5 mm behind (Fig. 15). The curve monotonicity is concurrent with the inlet velocity profile. Visible oscillations are present during the moments when the valve is moving, and are more apparent when the valve becomes fully closed or fully opened. The pressure drop peak was maximum for the 3^{rd} dataset and equals 0.40 kPa, where the mimimum peak equal 0.31 kPa was present in 4^{th} dataset. The exemplary curves for mentioned dataset models are presented in Fig. 15. Achieved results are close to the validated pressure drop values in [37,86–88], where pressure drops were on the level of 0.2 kPa to 1.0 kPa, dependent on the inlet velocity profile and vasculature geometry.

The blood flowing through the cardiac system exerts forces and stresses on the vessels and valves. They can be divided into two components: normal stress - pressure, and tangent stress - called wall shear stress (WSS). WSS values should fall below the appropriate limits, as too high shear stress (>40 Pa) may cause direct endothelial injury, and too low (<0.4 Pa) may lead to the arteriosclerotic plaque [89]. In the case of implanted valves, there is some risk of thromboembolism and thus patients are on long-term anticoagulant therapy [76,90]. The WSS in the valve vicinity is related to blood cell lysis and activation, which

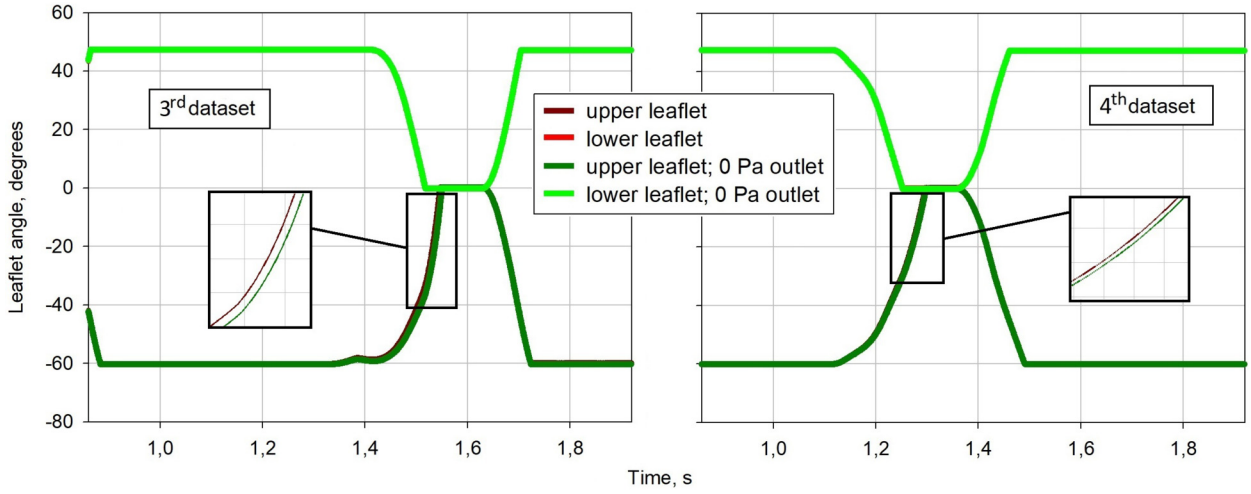

Fig. 11. Comparison of the leaflets angle time profiles, for the model including and excluding the outlet pressure variation in the input data. The differences in determined valve motion are negligible.

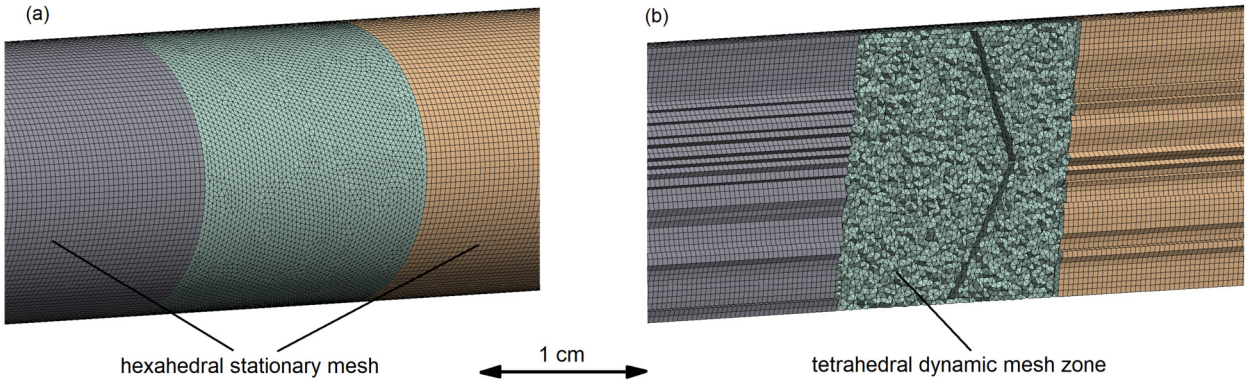

Fig. 12. Hybrid mesh prepared for the dynamic mesh approach, to compare the results obtained using overset method: **(a)** - outer mesh, **(b)** - cross-section through domain with visible gap in the fluid region created by the valve prosthesis.

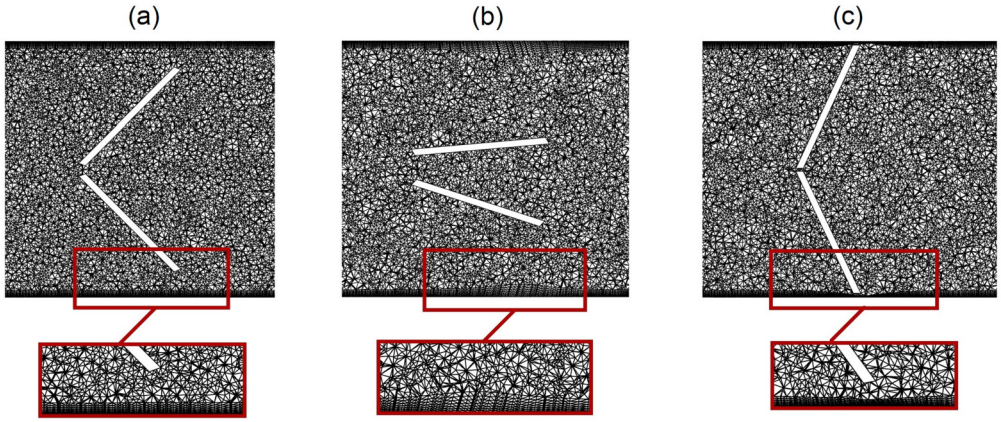

Fig. 13. Cross-section of the mesh prepared for the dynamic mesh approach: **(a)** the initial state, prior to the valve motion in domain, **(b)** the opened valve state with stretched boundary layer, **(c)** the closed valve state with compressed boundary layer. The remeshing process resulted in slightly decreased mesh density and the smoothing process visibly changed the thickness of the prism boundary layer, however the mesh quality was not deteriorated.

results in thrombi deposition in regions with stagnated flow [91]. Despite advances in hemodynamics, medical equipment and replacement, the problem of hemolysis, thrombus deposition and cavitation bubbles is still present with mechanical valves. High and low pressure values are present on both leaflets' sides at the edges, especially when the closed or opened state is achieved. The highest leaflets' pressure gradient, calculated as the difference between the maximum and minimum pressure exerted at their walls, was present during the maximum inlet velocity and was on the level of 2.5 kPa - see Fig. 16. Presented longitudinal and transverse cross-sections indicate high gradients, which could be successfully calculated with the described numerical mesh.

The WSS values are high in the time of increased inlet velocity and from the moments when the valve starts to close. The maximum value equals 54 Pa and it was achieved for the 2^{nd} dataset. As can be seen

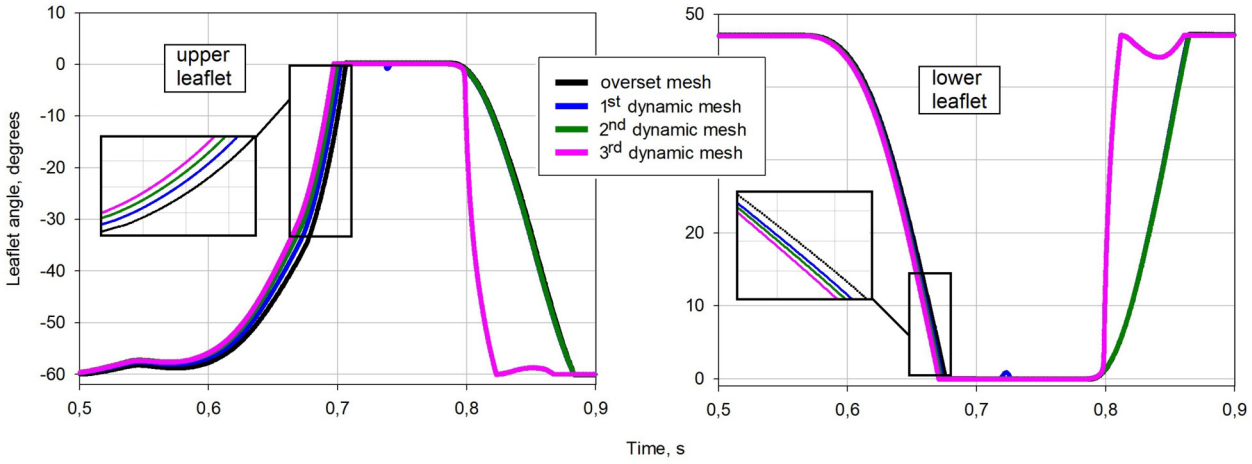

Fig. 14. Valve motion determined by the numerical model, with different moving mesh approaches applied. The *overset* approach result was compared here with results obtained by three different modules of *dynamic mesh* used instead. It is presented that only the result from the 3^{rd} approach (i.e., remeshing only) is disparate; however, this might be caused by the lack of prism boundary layer in this model.

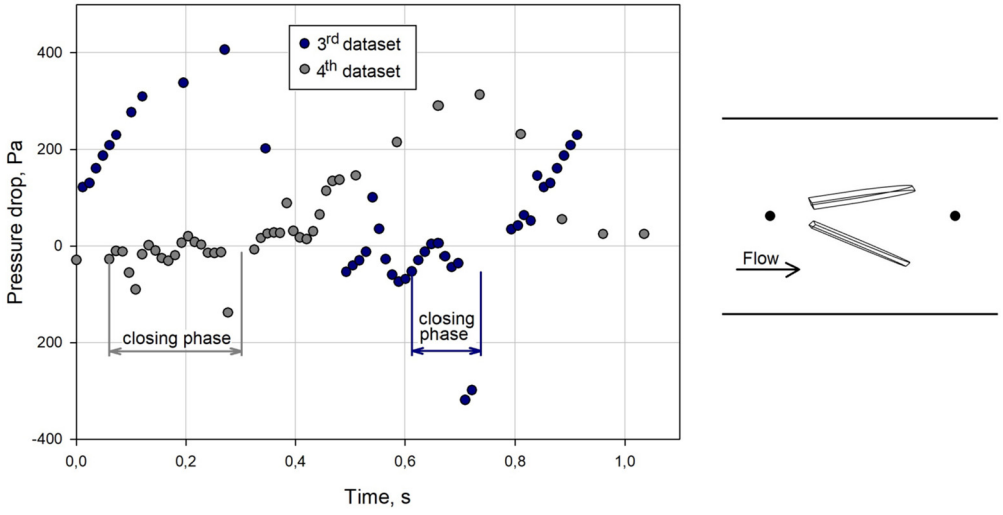

Fig. 15. Pressure drop past the valve prosthesis, calculated between two central points shown at the inset. Marked time intervals correspond to the valve closing phase. The pressure drop starts increasing when the fully closed valve state is achieved.

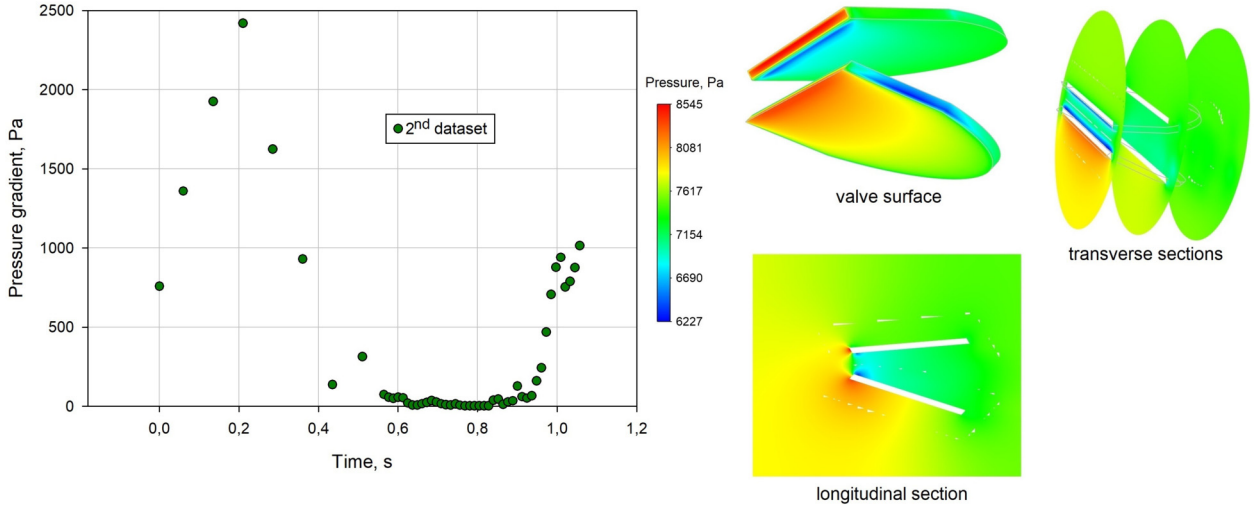

Fig. 16. Pressure gradient on the valve leaflets walls. The contours are presented for the time instant corresponding to the highest gradient. It is observed that in the region where fluid attacts the sharp surface, high pressure gradient is present; this might cause cavitation and leaflet deterioration over time.

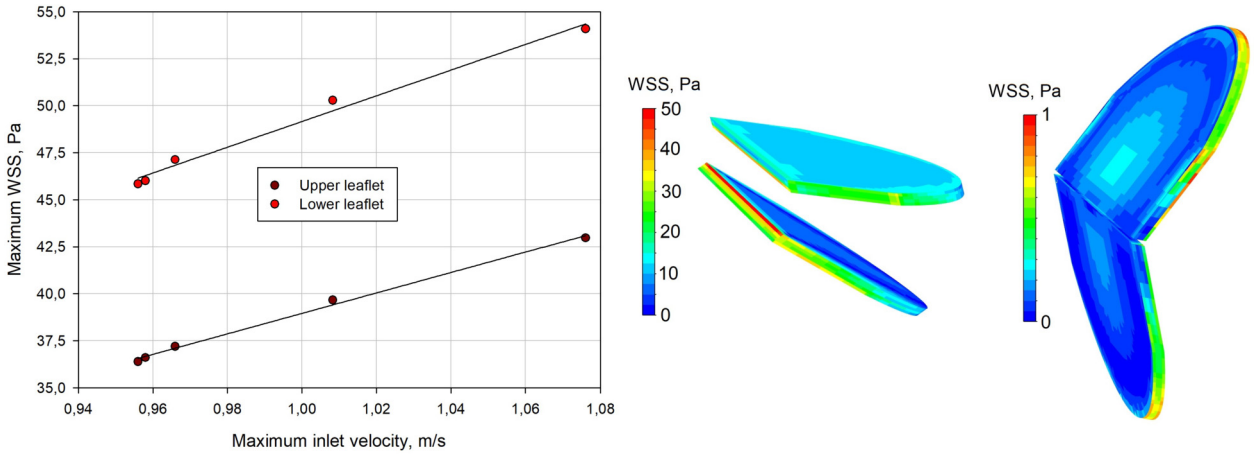

Fig. 17. The maximum wall shear stress on the valve walls, presented for all datasets, and correlated with the maximum inlet velocity. The contours presents the WSS during the closed and opened valve state. During the closed state, high values and gradients of WSS are present due to high fluid velocity, whereas for the closed state, WSS represents low values due to flow stagnation.

in Fig. 17, where the maximum wall shear stresses were correlated with the maximum inlet velocity in a given dataset, there is clear directly proportional dependence between the mentioned variables. Also, the values are higher for the lower leaflet for all datasets, which may be due to the upper leaflet is closer to parallel during opened state. As mentioned, high WSS values contribute to blood damage, lysis and platelet activation. This can happen when the values are on the level of 150-400 Pa [92], however, in the case of the presence of a foreign solid surface, much lower WSS values can cause hemolysis.

A common indicator used in the assessment of the aortic valve performance is the Effective Orifice Area (EOA). This coefficient is the measure of the effective valve opening during the forward flow phase and determines how well a valve design utilizes its primary orifice area. It is related to the degree to how the prosthesis itself obstructs the flow [76,93,94]. It can be calculated both experimentally and using simulation results, with an equation described by Gabbay, based on the principle of energy conservation [94]:

$$EOA = \frac{Q_{RMS}}{51.6\sqrt{\Delta \bar{p}}} \tag{18}$$

where EOA - effective orifice area (cm^2), 51.6 - gravitational constant, $\bar{p}$ - mean systolic pressure drop (mmHg) and Q_{RMS} - root mean square of the systolic flow rate (ml/s):

$$Q_{RMS} = \sqrt{\frac{1}{n}\sum_{i=1}^{n} Q_i^2} \tag{19}$$

where Q_i is the *i-th* measured mass flow rate value within the systolic phase of the heart cycle.

Valve stenosis results in low EOA values, resulting from the higher pressure loss and increased heart workload. The bileaflet type mechanical valve construction overcomes the drawback of low EOA values related to former mechanical valve types - caged-ball and ball-and-cage [93]. The EOA typically falls between the values $1.04 - 4.05$ cm^2 [76]. For the same construction type, it is proportional to the valve diameter and may vary in patients [95]. The measured value by [95] for the St Jude Medical® bileaflet valve equals 2.08 cm^2 and 3.23 cm^2 for size 21 mm and 25 mm, respectively. The calculated average value from five datasets simulations performed in our research was equal 2.73 cm^2 with standard deviation 0.05 cm^2, which indicates the appropriate prosthesis performance and almost constant EOA value, regardless what pressure, flow and cycle time conditions were applied.

Fig. 18 presents the velocity pathlines for 5^{th} dataset model. Five different time instants were considered: the moment when the valve started to open (0.312 s), the opening completion (0.429 s), the maximum inflow time (0.666 s), the closing start-up (0.128 s) and closing completion (0.189 s). As can be observed, the pathlines in the valve vicinity form irregular vorticity-like patterns, especially when the valve is moving. In the distance of several pipe diameters, the flow field becomes regular, no matter what leaflet angular positions are. During the opened state, a stable three-jet flow is achieved and remained, which can be stated by comparing 0.429 s and 0.666 s time stamps contours. During the closing, startup, and closed states, some minor regurgitation can be observed. Here, the velocity values are higher when the closing is completed, due to a small area of the leakage gap. Therefore, the regurgitation is not substantial, due to the fact that already small reversed velocity values instantly provoke valve closing, and the leakage area is small.

Fig. 19 presents the pressure exerted on the valve leaflets walls and the pressure gradient through the valve, on its vicinity, for 5^{th} dataset model. High gradients of the fluid pressure are observed, especially for the opening startup (0.312 s) and closing completion (0.189 s). The pressure values increasing or decreasing in the flow direction, indicate on the turn of the valve angular motion, i.e. opening or closing, accordingly. High pressure gradients are present on the leaflet walls in all time instants, resulted from the small flow gaps and also the fluid flowing around the sharp edges.

8. Summary and discussion

This paper presents the numerical model with in-house approach for FSI, for modeling structures rotating by the influence of fluid flow, as one-, two- or three-leaflet artificial valve. Two different moving mesh modules: overset mesh and dynamic mesh, were used and compared. Such comparison for artificial valves was not previously published. For the same mesh densities, both methods presented similar results, however the dynamic mesh method was more error-prone and demanded greater computational time due to the lower allowable mesh deformation per timestep. The model is realized in terms of six degrees of freedom rigid body motion. The novel approach for dynamic timestep sizing was here used and described, with analysis of different dynamic timestep constant values and it can influence onto solving time and moving mesh operation. Implementation of the module calculating timestep size appropriate to the determined leaflet velocity improved considerably the solver stability, moving mesh operation, and significantly reduced solving time by 72%.

The simulation results were validated with test rig measurements. The fast camera images were processed with usage of prepared application in Python OpenCV environment. The leaflet angle time courses determined by the numerical model fits the measurements within one

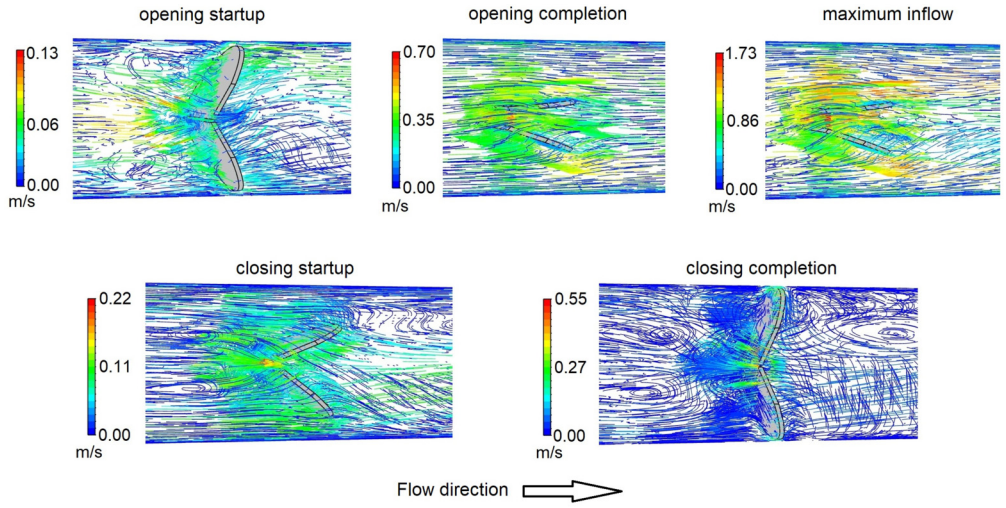

Fig. 18. Pathlines of velocity magnitude for model results of the 5^{th} dataset, presented for five different time instants. The valve motion causes visible eddies, whereas for the opened valve state, the three-jet flow can be observed.

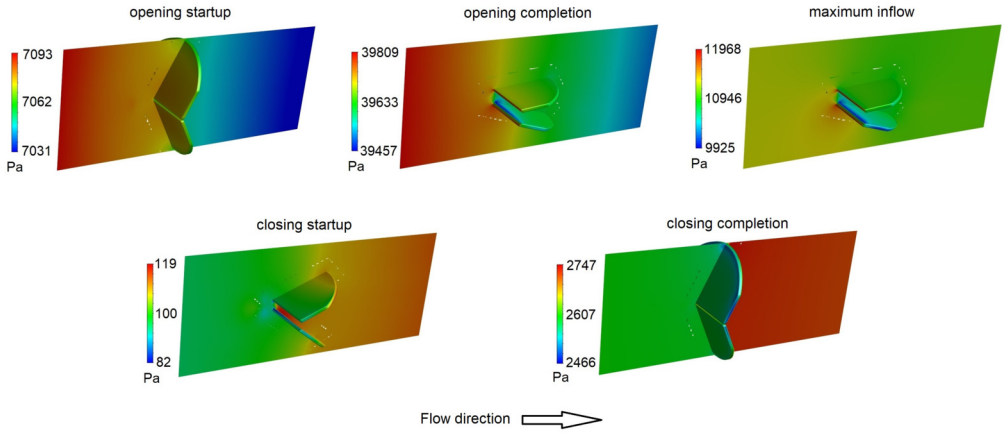

Fig. 19. Contours of the pressure exerted on the valve walls and on its central longitudinal section. Presented for model results of the 5^{th} dataset for five different time instants. Higher pressures before the valve promote its opening, whereas higher values past the valve promote its closing.

standard deviation, also good agreement was observed for the validated pressure values before the valve.

Multivariante analysis was performed considering the constant of the 6DOF model, the momentum of inertia. The model was shown to be quite insensitive to the momentum of inertia error, since the change in value at the level of $\pm 40\%$ did not affect significantly the valve leaflets angular motion, also even with less impact on other CFD characteristics.

The CFD results and the determined valve indicators indicate a proper valve operation in terms of effective orifice area, pressure drops, and regurgitation. Some typical phenomena for mechanical bileaflet valves are present, such as the rapid decrease of pressure exerted on leaflets' walls and high shear stresses that could effect in the cavitation bubbles or blood cell lysis, accordingly. The maximum pressure drop was on the level of 0.4 kPa. High gradients of pressure and WSS were present on the leaflet walls. The calculated EOA value indicated on the proper valve performance.

Interested readers are referred to the animations attached in the Appendix repository, where are depicted the valve motion, moving mesh operation, and fast camera images.

Credit authorship contribution statement

Marcin Nowak: Conceptualization, Data curation, Funding acquisition, Investigation, Methodology, Project administration, Resources, Software, Supervision, Validation, Visualization, Writing – original draft, Writing – review & editing. **Eduardo Divo:** Formal analysis, Writing – review & editing. **Tomasz Borkowski:** Investigation, Validation. **Ewelina Marciniak:** Investigation, Validation. **Marek Rojczyk:** Data curation, Investigation, Validation. **Ryszard Białecki:** Formal analysis, Funding acquisition, Project administration, Writing – review & editing.

Data availability

Data will be made available on request.

Acknowledgements

The financial support was provided by *National Science Centre*, Poland (project no. 2017/27/B/ST8/01046) and also by the grant ARGENTUM TRIGGERING RESEARCH GRANTS - 'Excellence Initiative - Research University', *Gdańsk University of Technology*, Gdańsk, Poland (project no. 32/1/2023/IDUB/I3b/Ag).
Computations were carried out using the computers of Centre of Informatics Tricity Academic Supercomputer & Network.

Appendix A. Supplementary material

Supplementary material related to this article can be found online at https://doi.org/10.1016/j.camwa.2024.09.010.

References

[1] E. Wilkins, L. Wilson, K. Wickramasinghe, P. Bhatnagar, J. Leal, R. Luengo-Fernandez, R. Burns, M. Rayner, N. Townsend, European Cardiovascular Disease Statistics, 2017 edition, European Heart Network, 2017.

[2] Z. Lasocka, Z. Lewicka-Potocka, A. Faran, L. Daniłowicz-Szymanowicz, R. Nowak, D. Kaufmann, A. Kaleta-Duss, L. Kalinowski, G. Raczak, E. Lewicka, A. Dąbrowska-Kugacka, Exercise-induced atrial remodeling in female amateur marathon runners assessed by three-dimensional and speckle tracking echocardiography, Front. Physiol. 13 (2022).

[3] A.M. Kaleta-Duss, Z. Lewicka-Potocka, A. Dąbrowska-Kugacka, G. Raczak, A. Siekierzycka, M. Woźniak, L. Kalinowski, E.K. Lewicka, Infammatory response to a marathon run in amateur athletes, Eur. J. Transl. Clin. Med. 4 (2021).

[4] R. Osnabrugge, D. Mylotte, S. Head, N. VanMieghem, V. Nkomo, C. LeReun, A. Bogers, N. Piazza, A. Kappetein, Aortic stenosis in the elderly: disease prevalence and number of candidates for transcatheter aortic valve replacement: a meta-analysis and modeling study, J. Am. Coll. Cardiol. 62 (11) (2013).

[5] J. Thaden, V. Nkomo, M. Enriquez-Sarano, The global burden of aortic stenosis, Prog. Cardiovasc. Dis. 55 (6) (2014) 565–571.

[6] R. Smith-Bindman, Is computed tomography safe, N. Engl. J. Med. 363 (1) (2010) 1–4.

[7] R. Smith-Bindman, D. Miglioretti, E. Johnson, C. Lee, H. Feigelson, M. Flynn, R. Greenlee, R. Kruger, M. Hornbrook, D. Roblin, et al., Use of diagnostic imaging studies and associated radiation exposure for patients enrolled in large integrated health care systems, J. Am. Med. Assoc. 307 (22) (2012).

[8] C. Storrs, How much do ct scans increase the risk of cancer, Sci. Am. 209 (1) (2013) 2400–2409.

[9] G.P. Chatzimavroudis, Blood flow measurements with magnetic resonance phase velocity mapping, Measurement 37 (2005).

[10] J. Malek, A.T. Azar, B. Nasralli, M. Tekari, H. Kamoun, R. Tourki, Computational analysis of blood flow in the retinal arteries and veins using fundus image, Comput. Math. Appl. 69 (2) (2015).

[11] Y. Qiao, J. Fan, K. Luo, Mechanism of blood flow energy loss in real healthy aorta using computational fluid-structure interaction framework, Int. J. Eng. Sci. 192 (2023).

[12] L. Radtke, M. König, A. Düster, The influence of geometric imperfections in cardiovascular fsi simulations, Comput. Math. Appl. 74 (7) (2017).

[13] M. Nobili, U. Morbiduccib, R. Ponzinic, C. Gaudiod, A. Balduccid, M. Grigionid, F. Montevecchib, A. Redaellia, Numerical simulation of the dynamics of a bileaflet prosthetic heart valve using a fluid-structure interaction approach, J. Biomech. 41 (2008).

[14] M. Kopernik, P. Koparczyk, Development of multi-phase models of blood flow for medium-sized vessels with stenosis, Acta Bioeng. Biomech. 21 (2019).

[15] M. Kopernik, A. Milenin, Two-scale finite element model of multilayer blood chamber of polvad_ext, Arch. Civ. Mech. Eng. 12 (2012).

[16] C.M. Augustin, M.A. Gsell, E. Karabelas, E. Willemen, F.W. Prinzen, J. Lumens, E.J. Vigmond, G. Plank, A computationally efficient physiologically comprehensive 3d–0d closed-loop model of the heart and circulation, Comput. Methods Appl. Mech. Eng. 386 (2021).

[17] Q. Hou, K. Tao, T. Du, H. Wei, H. Zhang, S. Chen, Y. Pan, A. Qiao, A computational analysis of potential aortic dilation induced by the hemodynamic effects of bicuspid aortic valve phenotypes, Comput. Methods Programs Biomed. 220 (2022).

[18] T.B. Domagala, A. Szeffler, L.W. Dobrucki, J. Dropinski, S. Polanski, M. Leszczynska-Wiloch, K. Kotula-Horowitz, J. Wojciechowski, L. Wojnowski, A. Szczeklik, L. Kalinowski, Nitric oxide production and endothelium-dependent vasorelaxation ameliorated by n1-methylnicotinamide in human blood vessels, Hypertension 59 (2012).

[19] A. Janaszak-Jasiecka, A. Siekierzycka, A. Płoska, I.T. Dobrucki, L. Kalinowski, Endothelial dysfunction driven by hypoxia - the influence of oxygen deficiency on no bioavailability, Biomolecules 11 (2021).

[20] A. Amindari, L. Saltik, K. Kirkkopru, M. Yacoub, H. Yalcin, Assessment of calcified aortic valve leaflet deformations and blood flow dynamics using fluid-structure interaction modeling, Inform. Med. Unlocked 9 (2017) 191–199.

[21] M. Bukač, S. Čanić, J. Tambača, Y. Wang, Fluid–structure interaction between pulsatile blood flow and a curved stented coronary artery on a beating heart: a four stent computational study, Comput. Methods Appl. Mech. Eng. 350 (2019).

[22] S.T. Ha, H.G. Choi, Semi-monolithic formulation based on a projection method for simulating fluid–structure interaction problems, Comput. Math. Appl. 134 (2023).

[23] C. Chnafa, S. Mendez, F. Nicoud, Image-based large-eddy simulation in a realistic left heart, Comput. Fluids 94 (2014) 173–187.

[24] Y. Imai, T. Omori, Y. Shimogonya, T. Yamaguchi, T. Ishikawa, Numerical methods for simulating blood flow at macro, micro, and multi scales, J. Biomech. 49 (2016) 2221–2228.

[25] L. Formaggia, A. Quarteroni, A. Veneziani, Cardiovascular Mathematics, 2009.

[26] F. Tajeddini, B. Firoozabadi, H.A. Pakravan, S.H. Ahmadi Tafti, Patient-specific fluid–structure interaction simulation of the lad-ita bypass graft for moderate and severe stenosis: a doubt on the fractional flow reserve-based decision, Biocybern. Biomed. Eng. 42 (2022).

[27] H. Yeh, O. Barannyk, D. Grecov, P. Oshkai, The influence of hematocrit on the hemodynamics of artificial heart valve using fluid-structure interaction analysis, Comput. Biol. Med. 110 (2019).

[28] L. Yanhong, A lattice Boltzmann model for blood flows, Appl. Math. Model. 36 (7) (2012) 2890–2899.

[29] S. Osaki, K. Hayashi, H. Kimura, T. Seta, E. Kohmura, A. Tomiyama, Numerical simulations of flows in cerebral aneurysms using the lattice Boltzmann method with single- and multiple-relaxation time collision models, Comput. Math. Appl. 78 (8) (2019).

[30] P. Eichler, R. Galabov, R. Fučík, K. Škardová, T. Oberhuber, P. Pauš, J. Tintěra, R. Chabiniok, Non-Newtonian turbulent flow through aortic phantom: experimental and computational study using magnetic resonance imaging and lattice Boltzmann method, Comput. Math. Appl. 136 (2023).

[31] T.B. Le, F. Sotiropoulos, Fluid-structure interaction of an aortic heart valve prosthesis driven by an animated anatomic left ventricle, J. Comput. Phys. 244 (2013) 41–62.

[32] H. Xing, G. Duckwiler, D. Valentino, Lattice Boltzmann simulation of cerebral artery hemodynamics, Comput. Fluids 38 (4) (2009) 789–796.

[33] R. Rama, S. Skatulla, Towards real-time modelling of passive and active behaviour of the human heart using podi-based model reduction, Comput. Struct. 232 (2020).

[34] U. Gulbulak, O. Gecgel, A. Ertas, A deep learning application to approximate the geometric orifice and coaptation areas of the polymeric heart valves under time-varying transvalvular pressure, J. Mech. Behav. Biomed. Mater. 117 (2021).

[35] M.A. Cruchaga, C.M. Muñoz, D.J. Celentano, Simulation and experimental validation of the motion of immersed rigid bodies in viscous flows, Comput. Methods Appl. Mech. Eng. 197 (33) (2008).

[36] M. de Tullio, G. Pedrizzetti, R. Verzicco, On the effect of aortic root geometry on the coronary entry-flow after a bileaflet mechanical heart valve implant: a numerical study, Acta Mech. 216 (1–4) (2011) 147–163.

[37] I. Borazjani, L. Ge, F. Sotiropoulos, High-resolution fluid-structure interaction simulations of flow through a bi-leaflet mechanical heart valve in an anatomic aorta, Ann. Biomed. Eng. 38 (2) (2010) 326–344.

[38] L. Dashi, L. Ge, H. Simon, F. Sotiropoulos, A. Yoganathan, Vorticity dynamics of a bileaflet mechanical heart valve in an axisymmetric aorta, Phys. Fluids 19 (2007).

[39] V. Govindarajan, H. Udaykumar, L. Herbertson, S. Deutsch, K. Manning, K. Chandran, Two-dimensional fsi simulation of closing dynamics of a tilting disc mechanical heart valve, J. Med. Devices 4 (2010).

[40] M. Tomaszewski, K. Sybilski, P. Baranowski, J. Małachowski, Experimental and numerical flow analysis through arteries with stent using particle image velocimetry and computational fluid dynamics method, Biocybern. Biomed. Eng. 40 (2020).

[41] M. Nowak, E. Divo, W. Adamczyk, Fluid-structure interaction methods for the progressive anatomical and artificial aortic valve stenosis, Int. J. Mech. Sci. 227 (2022).

[42] OpenCV library, v. 4.5.1-dev, online: https://opencv.org/releases, 2021.

[43] Efficient Split-Step Schemes for Fluid–Structure Interaction Involving Incompressible Generalised Newtonian Flows, Comput. Struct. 260 (2022).

[44] Medtronic® open pivot; instructions for use, https://europe.medtronic.com/xd-en/healthcare-professionals/products/cardiovascular/heart-valves-surgical/open-pivot-mechanical-heart-valve.html. (Accessed 1 August 2024).

[45] ANSYS® Academic Research, Release 17.2, Help System, ANSYS, Inc.

[46] E. Atta, Component - adaptive grid interfacing, in: AIAA 19th Aerospace Sciences Meeting, 1981.

[47] J. Benek, J. Steger, F. Dougherty, A flexible grid embedding technique with application to the Euler equations, in: AIAA Sixth CFD Conference, Danvers, MA, 1983.

[48] J. Benek, P. Buning, J. Steger, A 3-D Chimera grid embedding technique, AIAA seventh CFD conference, Cincinnati, OH. AIAA paper 85-1523, 1985.

[49] J. Benek, T. Donegan, N. Suhs, Extended Chimera grid embedding scheme with application to viscous flows, in: AIAA Eighth CFD Conference, Honolulu, HI, AIAA, 1987.

[50] D. Chandar, On overset interpolation strategies and conservation on unstructured grids in OpenFOAM, Comput. Phys. Commun. (2019).

[51] T.J. Baker, Mesh generation: art or science?, Prog. Aerosp. Sci. 41 (1) (2005) 29–63.

[52] J. Webster, Encyclopedia of Medical Devices and Instrumentation, second edition, John Wiley & Sons, Inc., Hoboken, New Jersey, 2007.

[53] M. Nobili, U. Morbiducci, R. Ponzini, C. Gaudio, A. Balducci, M. Grigioni, F. Montevecchi, A. Redaelli, Numerical simulation of the dynamics of a bileaflet prosthetic heart valve using a fluid-structure interaction approach, J. Biomech. 41 (2008) 2539–2550.

[54] J. Zhan, W. Cai, W. Hu, Y. Gong, T. Li, Numerical study on the six-DOF anchoring process of gravity anchor using a new mesh update strategy, Mar. Struct. 52 (2017) 173–187.

[55] M. Cengel, Y. Cimbala, Fluid Mechanics. Fundamentals and Applications, McGraw-Hill, 2006.

[56] F. White, Fluid Mechanics, McGraw-Hill, New York, 2010.

[57] P. Hoskins, P. Lawford, B. Doyle, Cardiovascular Biomechanics, Springer, 2017.

[58] Y. Bazilevs, K. Takizawa, T. Tezduyar, Computational Fluid-Structure Interaction, John Wiley & Sons, Ltd., Chichester, UK, 2013.

[59] T.B. Le, M. Usta, C. Aidun, A. Yoganathan, F. Sotiropoulos, Computational methods for fluid-structure interaction simulation of heart valves in patient-specific left heart anatomies, Fluids 7 (3) (2022).

[60] V. Govindarajan, H. Udaykumar, L. Herbertson, S. Deutsch, K. Manning, K. Chandran, Impact of design parameters on bi-leaflet mechanical heart valve flow dynamics, J. Heart Valve Dis. 18 (2009).

[61] C.J. Jordaan, Hydrodynamic and Coagulation Characteristics of a Re-Engineered Mechanical Heart Valve in an Ovine Model, Diss., University of the Free State, 2017.

[62] W. Polom, M. Migaczewski, J. Skokowski, M. Swierblewski, T. Cwalinski, L. Kalinowski, M. Pedziwiatr, M. Matuszewski, K. Polom, Multispectral imaging using fluorescent properties of indocyanine green and methylene blue in colorectal surgery - initial experience, J. Clin. Med. 11 (2022).

[63] M. Nowak, B. Melka, M. Rojczyk, M. Gracka, A. Nowak, A. Golda, W. Adamczyk, B. Isaac, R. Białecki, Z. Ostrowski, The protocol for using elastic wall model in modeling blood flow within human artery, Eur. J. Mech. B, Fluids 77 (2019) 273–280.
[64] Endress+Hauser, Proline Promag H 100 PROFIBUS DP. Operating instructions.
[65] Vision research, inc., https://www.phantomhighspeed.com/products/cameras/veo/veo710. (Accessed 27 September 2023).
[66] National instruments, inc., https://www.ni.com/pl-pl/shop/labview.html. (Accessed 27 September 2023).
[67] D. Lemos, A. Nunes, J. Machado, C. Barros, C. Leão, F. Soares, G. Minas, Mechanical simulation model of the systemic circulation, Measurement 66 (2015).
[68] S. Rumian, G. Milewski, M. Kopacz, S. Zamarlik, The possibility of the hydrodynamic evaluation of bio-pumps with the use of a hybrid-digital model of the circulatory system, Measurement 80 (2016).
[69] A. Widuch, K. Myöhänen, M. Nikku, M. Nowak, A. Klimanek, W. Adamczyk, Data set generation at novel test-rig for validation of numerical models for modeling granular flows, Int. J. Multiph. Flow 142 (2021).
[70] OpenCV documentation, v. 4.5.1-dev, online, https://docs.opencv.org/master/da/d22/tutorial_py_canny.html, 2021.
[71] A. Ratsakou, A. Skarlatos, C. Reboud, D. Lesselier, Shape reconstruction of delamination defects using thermographic infrared signals based on an enhanced canny approach, Infrared Phys. Technol. 111 (2020).
[72] A. Widuch, M. Nowak, D. Sukiennik, K. Myöhänen, M. Nikku, S. Shah, A. Parente, W. Adamczyk, Towards application of uncertainty quantification procedure combined with experimental procedure for assessment of the accuracy of the dem approach dedicated for granular flow modeling, Powder Technol. 399 (2022).
[73] M. Nowak, W. Adamczyk, B. Melka, Z. Ostrowski, R. Białecki, Numerical model of the aortic valve implanted within real human aorta, Adv. Intell. Syst. Comput. 1186 (2020).
[74] O. Zienkiewicz, R. Taylor, The Finite Element Method, fifth edition, The Basis, vol. 1, Butterworth Heinemann, 2000.
[75] ANSYS® v20.1, Discovery Spaceclaim. Displaying mass properties, ANSYS, Inc.
[76] J. Bronzino, The Biomedical Engineering HandBook, second edition, CRC Press LLC, 2000.
[77] O. Neikov, N. Yefimov, Handbook of Non-ferrous Metal Powders, second edition, Technologies and Applications, 2019.
[78] A. Bertram, R. Gluge, Solid Mechanics: Theory, Modeling and Problems, 2015.
[79] M. de Tullio, L. Afferrante, G. Demelio, G. Pascazio, R. Verzicco, Fluid–structure interaction of deformable aortic prostheses with a bileaflet mechanical valve, J. Biomech. 44 (2011).
[80] S. Annerel, S. Claessens, J. Degroote, P. Segers, J. Vierendeels, Validation of a numerical FSI simulation of an aortic BMHV by in vitro PIV experiments, Med. Eng. Phys. 36 (2014).
[81] C. Curgien, V. Deplano, E. Bertrand, Validation of a numerical 3-D fluid–structure interaction model for a prosthetic valve based on experimental PIV measurements, Med. Eng. Phys. 31 (2009).
[82] Ingress of Coolant Event Simulation with Trace Code with Accuracy Evaluation and Coupled Dakota Uncertainty Analysis, Fusion Eng. Des. 159 (2020) 111944.
[83] Y. Feng, R. Fu, B. Li, N. Li, H. Yang, J. Liu, Y. Liu, Prediction of fractional flow reserve based on reduced-order cardiovascular model, Comput. Methods Appl. Mech. Eng. 400 (2022).
[84] D. Carswell, D. McBride, T. Croft, A. Slone, M. Cross, G. Foster, A CFD model for the prediction of haemolysis in micro axial left ventricular assist devices, Appl. Math. Model. 37 (6) (2013) 4199–4207.
[85] E. Gudino, A. Sequiera, 3D mathematical model for blood flow and non-Fickian mass transport by a coronary drug-eluting stent, Appl. Math. Model. 46 (2017) 161–180.
[86] S. Kadhim, M. Nasif, H.A.-K. Hussain, A.-W. Rafat, Computational fluid dynamics simulation of blood flow profile and shear stresses in bileaflet mechanical heart valve by using monolithic approach, Simulation 94 (2) (2018) 93–104.
[87] M. Nobili, U. Morbiducci, R. Ponzini, C. Del Gaudio, A. Balducci, M. Grigioni, F. Maria Montevecchi, A. Redaelli, Numerical simulation of the dynamics of a bileaflet prosthetic heart valve using a fluid–structure interaction approach, J. Biomech. 41 (11) (2008) 2539–2550.
[88] T. Schaller, M. Scharfschwerdt, K. Schubert, C. Prinz, U. Lembke, H.-H. Sievers, Aortic valve replacement in sheep with a novel trileaflet mechanical heart valve prosthesis without anticoagulation, JTCVS Open 7 (2021) 76–88.
[89] A. Malek, S. Alper, S. Izumo, Hemodynamic shear stress and its role in atherosclerosis, J. Am. Med. Assoc. 282 (21) (1999) 2035–2042.
[90] T. Abe, K. Kamata, K. Kuwaki, K. Komatsu, S. Komatsu, Ten years' experience of aortic valve replacement with the omnicarbon valve prosthesis, Ann. Thorac. Surg. 61 (4) (1996) 1182–1187.
[91] K. Tashiro, Y. Shobayashi, A. Hotta, Numerical simulation of non-linear loading–unloading hysteresis behavior of blood clots, Biocybern. Biomed. Eng. 42 (2022).
[92] C. Nevaril, J. Hellums, C.A. Jr, E. Lynch, Physical effects in red blood cell trauma, AIChE J. 15 (707) (1969).
[93] A.P.Y. Lakshmi, P. Dasi, Helene A. Simon, Philippe Sucosky, Fluid mechanics of artificial heart valves, Clin. Exp. Pharmacol. Physiol. 36 (2) (2009) 225–237.
[94] R.J. Gray, A. Chaux, J.M. Matloff, M. DeRobertis, M. Raymond, M. Stewart, A. Yoganathan, Bileaflet, tilting disc and porcine aortic valve substitutes: in vivo hydrodynamic characteristics, J. Am. Coll. Cardiol. 3 (2) (1984) 321–327.
[95] O. Bech-Hanssen, K. Caidahl, I. Wallentin, P. Ask, B. Wranne, Assessment of effective orifice area of prosthetic aortic valves with Doppler echocardiography: an in vivo and in vitro study, J. Thorac. Cardiovasc. Surg. 122 (2) (2001) 287–295.